

1
2
3
4
5
6
7
8
9
10
11
12
13
14
15
16
17
18
19
20
21
22
23
24
25
26
27
28
29
30
31

**Assimilation of Radar Radial Velocity Data with the WRF Hybrid
Ensemble-3DVAR System for the Prediction of Hurricane Ike (2008)**

Yongzuo Li, Xuguang Wang, and Ming Xue

School of Meteorology and Center for Analysis and Prediction of Storms
University of Oklahoma, Norman, Oklahoma 73072

January, 2012

Submitted to Monthly Weather Review

Revised April 28, 2012

Corresponding author address:

Yongzuo Li
Center for Analysis and Prediction of Storms
University of Oklahoma,
120 David L. Boren Blvd, Norman OK 73072
yongzuo.li@ou.edu

32
33
34
35
36
37
38
39
40
41
42
43
44
45
46
47
48
49
50
51
52

Abstract

An enhanced version of the hybrid ensemble-3DVAR data assimilation system for the WRF model is applied to the assimilation of radial velocity (V_r) data from two coastal WSR-88D radars for the prediction of Hurricane Ike (2008) before and during its landfall. In this hybrid system, flow-dependent ensemble covariance is incorporated into the variational cost function using the extended control variable method. The analysis ensemble is generated by updating each forecast ensemble member with perturbed radar observations using the hybrid scheme itself. The V_r data are assimilated every 30 minutes for 3 hours immediately after Ike entered the coverage of the two coastal radars.

The hybrid method produces positive temperature increments indicating a warming of the inner-core throughout the depth of the hurricane. In contrast, the 3DVAR produces much weaker and smoother increments with negative values at the vortex center at lower levels. Wind forecasts from the hybrid analyses fit the observed radial velocity better than that from 3DVAR, and the 3-h accumulated precipitation forecasts from the hybrid are also more skillful. The track forecast is slightly improved by the hybrid method and slightly degraded by the 3DVAR compared to the forecast from the GFS analysis. All experiments assimilating the radar data show much improved intensity analyses and forecasts compared to the experiment without assimilating radar data. The better forecast of the hybrid indicates that the hybrid method produces dynamically more consistent state estimations. Little benefit of including the tuned static component of background error covariance in the hybrid is found.

53 **1. Introduction**

54 Tropical cyclones (TCs) are among the most costly forms of natural disaster (Pielke et al.
55 2008). An accurate TC forecast will require not only a numerical model to realistically simulate
56 both the TC itself and its environment, but also a data assimilation (DA) system that can
57 effectively use the observations to accurately estimate the initial TC vortex and the environment
58 where the TC is embedded in.

59 To address the TC initialization issue, many previous studies adopted the vortex
60 relocation and/or bogussing (e.g., Liu et al. 2000; Kurihara et al. 1995; Zou and Xiao 2000)
61 techniques. While such techniques are non-trivial and have been shown to improve the hurricane
62 forecast, how to maintain the dynamical and thermo-dynamical coherency of the hurricane and
63 its environment is probably the biggest challenge with such methods.

64 Recently, several studies have explored the use of ensemble-based DA methods to
65 initialize hurricane forecasts and have shown great promise (e.g., Torn and Hakim 2009; Zhang
66 et al. 2009; Li and Liu 2009; Hamill et al. 2011; Wang 2011; Weng et al. 2011; Zhang et al. 2011;
67 Aksoy et al. 2012; Weng et al. 2012; Dong and Xue 2012). The key with ensemble-based DA is
68 the use of an ensemble to estimate the forecast error statistics in a flow-dependent manner.
69 Therefore, the observation information will be properly weighted and spread consistent with the
70 background hurricane forecasts; and perhaps more importantly, the ensemble covariance can
71 realistically infer the flow-dependent cross-variable error statistics and therefore update state
72 variables not directly observed in a dynamically and thermodynamically consistent manner.

73 One candidate in ensemble-based DA is the hybrid ensemble-variational DA method. It
74 has been proposed (e.g., Hamill and Snyder 2000; Lorenc 2003; Etherton and Bishop 2004;
75 Zupanski 2005; Wang et al. 2007b, 2008a; Wang 2010), implemented and tested with numerical

76 weather prediction (NWP) models recently (e.g., Buehner 2005; Wang et al. 2008b; Liu et al.
77 2008, 2009; Buehner et al. 2010a,b; Wang 2011; Wang et al. 2011; Whitaker et al. 2011; Kleist
78 et al. 2011; Wang et al. 2012). A standard variational method (VAR) typically uses static
79 background error covariance, but a hybrid ensemble-variational DA system incorporates
80 ensemble-derived flow-dependent covariance into the VAR framework. The ensemble can be
81 generated by an ensemble Kalman filter (EnKF). Recent studies have suggested that hybrid DA
82 systems may represent the “best of both worlds” by combining the best aspects of the variational
83 and EnKF systems (e.g., Buehner 2005; Wang et al. 2007a, 2008a,b, 2009; Zhang et al. 2009;
84 Buehner et al. 2010ab; Wang 2010). While preliminary tests of the hybrid DA system with real
85 NWP models and data have shown great potential of the method for non-TC forecasts (e.g.,
86 Wang et al. 2008b; Buehner et al. 2010ab) and for forecasts of TC tracks (e.g., Wang 2011;
87 Whitaker et al. 2011), and there has been a growing body of literature documenting the success
88 of using the EnKF to assimilate inner core data for TC initialization at convection-allowing
89 resolutions (e.g., Zhang et al. 2009, Weng et al. 2011; Zhang et al. 2011; Aksoy et al. 2012;
90 Weng et al. 2012; Dong and Xue 2012), to the author’s best knowledge, to date there is no
91 published study applying a hybrid DA method to the assimilation of radar data at a convection-
92 allowing resolution for TC predictions. This study serves as a pilot study applying the hybrid
93 ensemble-3DVAR system developed for the WRF model (Wang et al. 2008a) to explore its
94 potential for assimilating radar observations for hurricane forecasts. As a first step of such study,
95 we focus on assimilating radar radial velocity data. Meanwhile, this study also performs detailed
96 diagnostics to understand the fundamental differences between the roles and effects of flow-
97 dependent and static covariances in the TC analysis and forecast.

98 More specifically, this study applies and explores the WRF ensemble-3DVAR hybrid
99 system to the assimilation of coastal WSR-88D radar radial velocity data for the prediction of
100 Hurricane Ike (2008) (Fig. 1). Ike is the second costliest tropical cyclones in the recorded history
101 (1900-2010) over the mainland United States (<http://www.nhc.noaa.gov/pdf/nws-nhc-6.pdf>).
102 Previous studies (e.g., Zhao and Xue 2009) have shown significant impact of the radar data for
103 this case using ARPS 3DVAR/cloud analysis package. The remainder of this paper is organized
104 as follows: Section 2 presents the methodology and section 3 discusses the experiment design.
105 The experiment results are discussed in Section 4 while the final section summarizes the main
106 conclusions of this study.

107 **2. Methodology**

108 *a. The hybrid ensemble-3DVAR scheme*

109 A diagram of the hybrid DA system is shown in Fig. 2. Similar to Hamill and Snyder
110 (2000), the following four steps are repeated for each DA cycle: 1. Perform K (K is the ensemble
111 size) number of ensemble forecasts to generate background forecast fields at the time of analysis;
112 2. Calculate ensemble forecast perturbations to be used by the hybrid cost function for flow-
113 dependent covariance by subtracting ensemble mean from each member; 3. Generate K
114 independent sets of perturbed observations by adding random perturbations to the observations; 4.
115 Obtain the analysis increment for each ensemble member through minimization of the hybrid
116 cost function using one set of perturbed observations. Steps 1 through 4 are repeated for each of
117 the follow-on cycles, with the ensemble analyses providing initial conditions for step 1. In step 3,
118 the random perturbations added to the observations are drawn from a Gaussian distribution with
119 a mean of zero and a standard deviation of the observation error. This ‘perturbed observation
120 method’ was used in Hamill and Snyder (2000), which corresponds to the classic stochastic

121 ensemble Kalman filters (Burgers et al. 1998; Houtekamer and Mitchell 1998; Evensen, 2003).
 122 In the original work of Wang et al. (2008a), the ensemble transform Kalman filter (ETKF) was
 123 used to update forecast perturbations.

124 A brief review on the extended control variable method for incorporating ensemble
 125 covariance into a WRF 3DVAR framework is given here. For detailed discussions, readers are
 126 referred to Wang et al. (2007b, 2008a).

127 For state vector \mathbf{x} , the analysis increment of the hybrid scheme, \mathbf{x}' , is the sum of two
 128 terms,

$$129 \quad \mathbf{x}' = \mathbf{x}'_1 + \sum_{k=1}^K (\mathbf{a}_k \circ \mathbf{x}_k^e). \quad (1)$$

130 The first term \mathbf{x}'_1 in Eq. (1) is the increment associated with WRF 3DVAR static background
 131 covariance and the second term is the increment associated with flow-dependent covariance.
 132 Here, the vectors \mathbf{a}_k , $k = 1, \dots, K$, denote extended control variable (Lorenc 2003) for each
 133 ensemble member; and the second term of Eq. (1) represents a local linear combination of
 134 ensemble perturbations. The coefficient \mathbf{a}_k for each member varies in space as discussed later,
 135 which determines the ensemble covariance localization (see Wang et al. 2008a for further
 136 details). \mathbf{x}_k^e is the k^{th} ensemble perturbation state vector. The symbol 'o' denotes the Schur
 137 product (element by element product) of the vectors \mathbf{a}_k and \mathbf{x}_k^e .

138 The cost function for WRF hybrid ensemble-3DVAR is

$$139 \quad J(\mathbf{x}'_1, \mathbf{a}) = \beta_1 J_b + \beta_2 J_e + J_o,$$

$$140 \quad = \beta_1 \frac{1}{2} (\mathbf{x}'_1)^T \mathbf{B}^{-1} (\mathbf{x}'_1) + \beta_2 \frac{1}{2} (\mathbf{a})^T \mathbf{A}^{-1} (\mathbf{a}) + \frac{1}{2} (\mathbf{y}^{o'} - \mathbf{H}\mathbf{x}')^T \mathbf{R}^{-1} (\mathbf{y}^{o'} - \mathbf{H}\mathbf{x}'). \quad (2)$$

141 J_b is the traditional WRF 3DVAR background term associated with the static covariance \mathbf{B} and
 142 J_e is the hybrid term associated with flow-dependent covariance. \mathbf{a} is defined as

143 $\mathbf{a}^T = (\mathbf{a}_1^T, \mathbf{a}_2^T, \dots, \mathbf{a}_k^T)$. J_o is the observation term associated with observation error covariance \mathbf{R} .

144 The innovation vector $\mathbf{y}^{o'}$ is defined as, $\mathbf{y}^{o'} = \mathbf{y}^o - \mathbf{H}(\mathbf{x}^b)$, where \mathbf{y}^o is the observation vector, \mathbf{x}^b is
145 the background forecast state vector, and \mathbf{H} is the linearized observation operator.

146 The weights of the static covariance and flow-dependent covariance are determined by
147 factors β_1 and β_2 according to relationship

$$148 \quad \frac{1}{\beta_1} + \frac{1}{\beta_2} = 1, \quad (3)$$

149 which conserves the total variance.

150 As described in Wang et al. (2008a), the ensemble covariance localization, denoted as \mathbf{A} ,
151 has horizontal and vertical components. In this study, both the horizontal and vertical
152 localization are applied. Specifically, the horizontal localization is modeled by a recursive filter
153 transform as in Wang et al. (2008a). The vertical localization is implemented by transforming the
154 extended control variable \mathbf{a} in Eq. (2) with empirical orthogonal functions (EOFs). The
155 correlation matrix, denoted as Cov, from which the EOFs is derived, follows

$$156 \quad \text{Cov}(k_1, k_2) = \exp\left(-\frac{d^2}{L^2}\right), \quad (4)$$

157 where d is the distance between model levels k_1 and k_2 and L is the vertical localization radius.
158 Existing EOF codes in the WRF 3DVAR for modeling the vertical static error covariance is used
159 for the vertical ensemble covariance localization purpose.

160 **3. Experimental design**

161 *a. The WRF model configuration*

162 The Advanced Research WRF (ARW) model version 3 (Skamarock et al. 2008) is used
163 in this study. The model is compressible, three-dimensional, non-hydrostatic, discretized on a

164 Arakawa C grid with terrain-following mass-based sigma coordinate levels. In this study, the
165 WRF model is configured with 401x401 horizontal grid points at 5-km grid spacing (Fig. 1), and
166 41 vertical levels with the model top at 100 hPa. The WRF single-moment six-class scheme
167 (Hong et al. 2004) is chosen for the explicit microphysics processes. Since the grid resolution
168 may not fully resolve the hurricane convective features, the Grell-Devenyi cumulus
169 parameterization scheme (Grell; Devenyi 2002) is included. Other physics parameterizations
170 schemes used include the Yonsei University (YSU) (Noh et al. 2003) scheme for planetary
171 boundary layer parameterization, the 5-layer thermal diffusion model for land surface processes
172 (Skamarock et al. 2008), the Rapid Radiative Transfer Model (RRTM) longwave (Mlawer et al.
173 1997), and the MM5 shortwave (Dudhia 1989) radiation parameterization.

174 *b. The radar data processing*

175 The radial velocity data from coastal WSR-88D radars at Houston, Texas (KHGX) and
176 Lake Charles, Louisiana (KLCH) are processed using a modified version of the Four
177 Dimensional Dealiasing Algorithm (James and Houze 2001). The algorithm was originally
178 designed for Doppler radars in European Alps. The modified algorithm by this study is capable
179 of reading level-II WSR-88D data and dealiasing the radial velocities.

180 To dealias radial velocity data, the following steps are performed: First, a wind profile is
181 created based on model background, rawinsonde, or wind profiler data. The background radial
182 velocity in radar observation space is calculated from the wind profile, assuming the wind is
183 horizontally homogeneous. Second, the WSR-88D radial velocity is compared with the
184 background radial velocity for a gross check. In this step, aliased radial velocity that needs to be
185 corrected is identified. Third, at each elevation angle, spatial dealiasing is performed. The aliased
186 velocity V_a will be recovered by factored Nyquist velocity V_n ,

187
$$V_d = V_a + 2NV_n, \quad (5)$$

188 where N is a positive or negative integer whose sign and value are determined by a gate-to-gate
189 shear threshold of $0.4V_n$ (James and Houze 2001). After dealiasing is finished, the radial velocity
190 interpolated to the Cartesian coordinates is thinned to 10 km spacing horizontally and 500 meter
191 vertically.

192 Figure 3 shows the processed radial velocity at 0.5° elevation angle for KHGX (Fig. 3a)
193 and KLCH (Fig. 3b) at 0000 UTC 13 September 2008. These two radars complement each other
194 by providing scans that are approximately the right angle at the location of Ike's eye. KHGX
195 covers almost all of Ike's eye and eye wall. The outbound radial velocity on the left side of the
196 eye and inbound radial velocity on the right side of the eye reflect the circulation of the hurricane.
197 KLCH covers only about half of eye and eye wall. The outbound radial velocity on the front side
198 of the eye and inbound radial velocity on the back side of the eye also reflect the circulation of
199 the hurricane.

200 The observation error standard deviation for the radial velocity is set to 2 m s^{-1} during the
201 DA. This error value is similar to the values used in (Dowell; Wicker 2009), (Xu; Gong 2003),
202 and (Xiao et al. 2009).

203 *c. The data assimilation setup*

204 This paper presents five experiments denoted as NoDA, 3DVARa, 3DVARb, HybridF,
205 and HybridH (Table 1). Experiments differ based on what, if any, assimilation system is used for
206 radar data. The experiments are designed to examine the difference of using flow-dependent
207 versus static background covariance when assimilating the radar data and the impact of DA on
208 the subsequent forecast.

209 The NoDA experiment did not assimilate any radar data, instead the WRF model initial
210 condition at 0300 UTC 13 September 2008 simply comes from the 1°x1° degree NCEP (National
211 Centers for Environmental Prediction) operational GFS (Global Forecast System) analysis. The
212 6-hourly GFS analyses also provide the lateral boundary conditions (LBCs).

213 The “3DVARb” experiment assimilated the radar data using the traditional 3DVAR
214 method where the static background covariance is adopted. The static covariance is generated
215 and further tuned as followed. The NMC method (Parrish and Derber 1992) was first employed
216 to generate the static background covariance statistics based on 12-h and 24-h WRF model
217 forecasts, starting at 00 UTC and 12 UTC every day, during the period from 01 to 15 September
218 2008. The experiment using the static covariance generated by the above procedure without
219 further tuning is denoted as 3DVARa. Because the default correlation length scales derived from
220 the NMC method reflects mostly large-scale error structures, their direct use may not be
221 appropriate for storm-scale radar DA (Liu et al. 2005). The horizontal correlation length scale of
222 the static covariance is reduced by a factor of 0.3 in experiment 3DVARb and this factor is found
223 to be optimal through experimentations. The 3DVAR experiments contains three stages (Fig.
224 4a): (1) a single 6-h spinup forecast initialized from the GFS analysis at 1800 UTC, September
225 12, to produce an initial first guess at 0000 UTC, September 13 for radar DA cycles. The spin-up
226 time of 6 hours is based on past experiences and other published studies (e.g., Zhang et al. 2009,
227 spin-up time of 9 hours; Aksoy et al. 2012, spin-up time of 6 hours); (2) assimilation of radial
228 velocity data from KHGX and KLCH radars every 30 minutes for 3 hours; (3) a 21-h
229 deterministic forecast initialized by the analysis at the end of the assimilation cycles in (2). The
230 WRF model boundary conditions for all three stages are also provided by the operational GFS

231 analyses at 6 hourly intervals. Experiment 3DVARb serves as a base line for evaluating the
232 performance of the hybrid method.

233 Experiments HybridF and HybridH are identical except that the different weighting
234 factors β_1 and β_2 are used in Eq. (2). For HybridF, the full weight is assigned on the flow-
235 dependent ensemble covariance (using $1/\beta_1 = 1/1001$ and $1/\beta_2 = 1/1.001$). For HybridH, the static
236 covariance and the flow-dependent ensemble covariance are equally weighted ($1/\beta_1 = 1/2$ and
237 $1/\beta_2 = 1/2$), i.e., only half of the flow-dependent covariance is used, hence the ‘H’ in the name.
238 The horizontal correlation scale of static covariance in HybridH is also reduced by a factor of 0.3
239 as in 3DVARb. Meanwhile, HybridH uses the same flow dependent covariance localization as
240 HybridF, which will be discussed in detail in section 4.a.

241 Each of the hybrid experiments, HybridF and HybridH, has 40 ensemble members.
242 Similar to the 3DVAR experiments, the hybrid experiments have three stages (Fig. 4b): (1) 6-h
243 ensemble forecasts to spin up a first guess ensemble and provide flow-dependent covariance at
244 the beginning of the radar DA cycles. The initial and boundary conditions for each member are
245 the GFS analysis plus correlated random perturbations following Torn et al. (2006) and Wang et
246 al. (2008a,b); (2) assimilation of perturbed radial velocity data from KHGX and KLCH radars
247 every 30 minutes for 3 hours by variationally minimizing the hybrid cost function, according to
248 the description given in the previous section (see also Fig. 2); (3) a 21-h deterministic forecast
249 initialized from the ensemble mean analysis at the end of the DA cycles in (2). To generate the
250 random perturbations in (1), the random-cv facility in the WRF 3DVAR system is employed
251 (Barker et al. 2004). First, a random control variable vector is created with a normal distribution
252 having a zero mean and unit standard deviation. Then the perturbation control variable vector is
253 transformed to the model space to obtain perturbations to the model state variables including the

254 horizontal wind components, pressure, potential temperature, and mixing ratio of water vapor.
255 The perturbation standard deviations are roughly 1.9 m s^{-1} for the horizontal wind components,
256 0.6 K for temperature, 0.3 hPa for model pressure perturbation, and 0.9 g kg^{-1} for water vapor
257 mixing ratio and these values are based on the NMC-method-derived background error statistics.

258 Like other ensemble based data assimilation algorithm, the hybrid ensemble-3DVAR
259 quickly reduces ensemble spread after assimilating observations. The relaxation method of
260 Zhang et al. (2004) for ensemble covariance inflation was adopted. Specifically, the inflated
261 ensemble posterior perturbation \mathbf{x}'_{new} is a weighted average of prior perturbation \mathbf{x}'_f and posterior
262 perturbation \mathbf{x}'_a , $\mathbf{x}'_{\text{new}} = (1 - b) \mathbf{x}'_f + b \mathbf{x}'_a$, the relaxation coefficient, denoted as b , is set to 0.5 in
263 this study. This formulation retains part of prior perturbation to mitigate quick spread reduction.

264 **4. Results and discussion**

265 The analysis increment of the first DA cycle, the cycling process, the final analysis fields,
266 and the deterministic forecasting results will be presented and discussed in this section. The
267 subsection organization roughly follows the experiment flow charts in Fig. 4.

268 *a. Single observation test for vertical localization*

269 Before complete DA experiments are performed, the vertical covariance localization in
270 the hybrid scheme is tested by assimilating a single radial velocity observation. Figure 5 shows
271 the wind speed increment produced by HybridF analyzing a single radial velocity observation
272 located 3176 m above sea level at 0000 UTC 13 September 2008. The innovation (i.e., the
273 observed radial velocity minus forecast ensemble mean valid at 0000 UTC 13 September) for
274 this observation is -38.63 m s^{-1} . Without the vertical localization, nonzero increment reaches the
275 top of the model with relatively noisy increments at the upper levels (Fig. 5a). The horizontal and
276 vertical localization radii of 60 and 3 km, respectively, are used in hybrid experiment HybridF

277 (and in HybridH). The localization radii were empirically determined. For example, we tested 20
278 km, 60km, 200 km, 600 km for horizontal localization and found the 60km showed the most
279 reasonable increment. The vertical localization was also tested. The radar observation over Ike
280 inner core area is about 3 km above the surface. With 3 km vertical localization scale, the
281 influence of radar data could reach the surface. Figure 5b shows that with such localizations, the
282 analysis increment is more confined around the observation location. This single observation test
283 shows that our implementation of the vertical localization is taking effect.

284 *b. Wind increments*

285 To see the differences in analyzing the radar data using flow-dependent and static
286 covariances, the analysis increments from the 3DVAR and hybrid experiments after the first
287 analysis time are compared. We first look at the wind increments and will look at indirectly
288 related cross-variable increments in the next subsection.

289 Figure 6 shows the wind analysis increments at 850 hPa, at 0000 UTC 13 September
290 2008, the time of first analysis for 3DVARa, 3DVARb, HybridF, and HybridH. The increment in
291 3DVARa using the default NMC-method-derived static covariance shows cyclonic and anti-
292 cyclonic increment patterns of rather large scales (Fig. 6a); the cyclonic increment circulation is
293 centered almost 2 degrees off the observation hurricane center to the southsoutheast, while at the
294 hurricane center location the wind increment is mostly easterly. To the north the increment
295 circulation shows an anti-cyclonic pattern. Such cyclonic and anti-cyclonic increments are also
296 found in a previous studies assimilating radar radial velocity data using WRF 3DVAR (e.g., Xiao
297 et al. 2007), but are clearly unrealistic, and do not reflect the fact that a strong vortex exists
298 where the background strongly underestimate the strength of the vortex. The default background
299 error covariance derived from the NMC method is unaware of the hurricane vortex and its spatial

300 correlation scales mostly reflect synoptic scale error structures. The net result is the
301 inappropriately large amount of smoothing of the radar data in the data dense region and
302 inappropriately large spreading of the information outside the data coverage region. The radar
303 data, being collected at high spatial resolution, should be analyzed using much smaller spatial
304 correlation scales. This had been pointed out in Liu et al. (2005). The use of smaller correlation
305 scales for radar data is a common practice in the ARPS 3DVAR system (e.g., Hu et al. 2006;
306 Schenkman et al. 2011). Sugimoto et al (2009) also tested the sensitivity of WRF 3DVAR to the
307 correlation length scale and the variance of the background covariance for radar data assimilation.

308 In 3DVARb, the default horizontal spatial correlation scale is reduced by a factor of 0.3.
309 The resulting wind increment now shows a more or less symmetric cyclonic pattern around the
310 observed center of Ike (Fig. 6b). Compared with 3DVARa, the large increments are more limited
311 to the region of vortex in 3DVARb, and the increment is consistent with the inbound and
312 outbound radial velocity couplets associated with the hurricane vortex as observed by KHGX
313 and KLCH radars (Fig. 3). Such results are more realistic.

314 In HybridF with full weight given to the flow-dependent covariance, the wind increment
315 also shows a cyclonic pattern centered around the eye of Ike (Fig. 6c), but the increment
316 circulation is less axisymmetric, reflecting the contribution of spatially inhomogeneous flow-
317 dependent covariance. When equal weights are placed on the ensemble covariance and static
318 covariance in HybridH, the wind increments show a pattern that is close to that of 3DVARb, but
319 the increment magnitude is between those of the HybridF and 3DVARb (Fig. 6d).

320 *c. Temperature increments*

321 Because radar radial velocity is the only data type assimilated in this study, any
322 increment in temperature is the result of balance relationship applied (if any) and/or due to cross-

323 covariance in the background error. Figure 7 shows the 850 hPa temperature increments for
324 3DVARb, HybridF, and HybridH after assimilating radial velocity data for the first cycle. For
325 3DVARb, negative temperature increments are found in the vortex region, and the magnitude is
326 largest near the hurricane center (Fig. 7a). Physically, enhanced hurricane vortex circulation
327 should be accompanied by warming of the vortex core region, to give a warmer core vortex;
328 hence the 3DVAR temperature increment is inconsistent with expected hurricane structures. The
329 negative increment is expected of the 3DVAR, because the increment is obtained through a
330 balance relationship between temperature and wind and this relationship reflects the thermal
331 wind relation. More specifically, the ‘balanced temperature’ increment T_b at a vertical level k , in
332 WRF 3DVAR is related to the stream function ψ by a regression relation, $T_b(k) = \sum_l G(l,k) \psi(l)$,
333 where G is the regression coefficient and the summation is over the vertical index l . Such a
334 regression relation derived using the NMC-method generally reflects hydrostatic, geostrophic,
335 and thermal wind relations (Barker et al. 2004). A colder core at 850 hPa is consistent with an
336 enhanced cyclonic circulation at the 700 hPa seen in Fig. 6. Note that at this distance, the lowest
337 radar beams do not reach below 850 hPa, hence the enhancement of wind is larger above 850
338 hPa. Therefore the cyclonic wind increment increases with height in the lower atmosphere. We
339 note that negative temperature increment is also seen in the low-level eye region of analyzed
340 hurricanes in previous studies using Airborne Doppler radar data and WRF 3DVAR (e.g., Xiao
341 et al. 2009)

342 Different from 3DVAR, the temperature increment obtained in HybridF shows positive
343 increments in the eye region (Fig. 7b) and spiral patterns in the eye wall and outer rainband
344 regions. In this case, the hurricane in the background forecast at 0000 UTC 13 September 2008
345 is much weaker than the observation (Fig. 8b), which is accompanied by lower temperatures at

346 the core of the vortex than observed. When radar observations are assimilated, the background
347 TC vortex is strengthened and therefore the core temperature is expected to be increased to be
348 consistent with the warm core structure of TCs. The more realistic increment structures in
349 HybridF are the result of temperature-wind cross covariances derived from the ensemble, which
350 have knowledge of the vortex as a tropical cyclone. In addition, the magnitude of the temperature
351 increments in HybridF is an order of magnitude larger than that of 3DVARb; the temperature
352 increment in the 3DVAR analysis of Xiao et al. (2009) for Hurricane Jeanne (2004) was also
353 weak, reflecting the relative weak thermal wind relationship in 3DVAR.

354 Same as the wind increment, the temperature increment from HybridH is in-between
355 those of HybridF and 3DVARb (Fig. 7c). The magnitude is about half that of HybridF. The
356 structure of the increment resembles that of HybridF more but the eye region has negative
357 instead of positive increments. From this aspect, HybridH is poorer than HybridF.

358 *d. Innovation statistics for Vr and minimum sea level pressure in DA cycles*

359 The behaviors of 3DVARb, HybridH, and HybridF are further compared by examining
360 the fit of their analyses and forecasts to Vr observations during the DA cycles. The fit is defined
361 as the root mean square difference (RMSD) between the model state and observations, after the
362 model state is converted to the observed quantities; and such difference is also called observation
363 innovation. Figure 8 shows the RMSDs for Vr and minimum sea level pressure (MSLP) from
364 HybridH, HybridF and 3DVARb. Vr data of both KHGX and KLCH are used in the innovation
365 calculation and for the hybrid, the ensemble mean is used. In all three experiments, the RMSD
366 for Vr is reduced significantly by the analysis within each cycle and the largest reduction occurs
367 in the first analysis cycle at 0000 UTC when the observation innovations are the greatest. In later
368 cycles, the innovations for the analyses remain roughly between 2.5 and 3.5 m s⁻¹, which is

369 reasonable given the 2 m s^{-1} expected observation error. The 30-minute forecasts following each
370 analysis generally increase the V_r innovation by about 2 m s^{-1} , reaching $4\text{-}5 \text{ m s}^{-1}$ levels. In
371 general, HybridH produces analyses that fit V_r observations tightest while HybridF the least and
372 3DVARb is in-between. Similar is true of the 30-minute forecasts. Note that although the
373 analysis increment of HybridH is in general (Fig. 6 and Fig. 7) in-between HybridF and
374 3DVARb, the root-mean-square V_r fit to observations in HybridH is not necessarily between
375 HybridF and 3DVARb. The observation innovation statistics can help us to see if the DA system
376 is doing about the right things, but being ‘verification’ against the same set of observations that
377 is also used in the DA, it cannot really tell us the true quality of the analyses. True measures of
378 the analysis quality require verifications against independent observations or verification of
379 subsequent forecasts, which will be presented later.

380 Figure 8b shows the fit of the analysis and forecast MSLPs to the best track data from the
381 National Hurricane Center. The best track MSLP is more or less constant during this 3 hour
382 period, being at about 952 hPa. At the beginning of DA cycling (0000 UTC 13 September), the
383 MSLP is about 23 hPa higher than the best track estimate. Most of the reductions in MSLP in all
384 cases are actually achieved through adjustment during the forecasting process, with more than 15
385 hPa reduction achieved during the first analysis cycle between 0000 and 0030 UTC. This is not
386 surprising because wind is the only parameter directly measured, and pressure analysis
387 increments are only achieved through balance relationships and/or cross covariance, which are
388 apparently weak.

389 We note in general, the MSLP decreases faster in the short forecasts between the analyses
390 in the hybrid experiments than in 3DVARb. This is consistent with the fact that the hybrid
391 method tends to build a warmer vortex core, and warmer temperature tends to induce a lower

392 surface pressure due to hydrostatic balance. A stronger vortex circulation will also induce lower
393 central pressure due to cyclostrophic balance. During the final 3 cycles, there is clearly over-
394 deepening of the central pressure in HybridH in the short forecasts, resulting in a fall of MSLP
395 that is about 5.5 hPa too low compared to best track. The final analyzed MSLP in HybridF is
396 about 2.0 hPa too low, which should be within the uncertainty range of MSLP best track data.
397 We also note that in this study, since the dense radar data define the TC center location rather
398 well (Fig. 3) and are assimilated every 30 minutes, the TC locations in the first guess ensembles
399 do not diverge too much in the 30-minute forecasts throughout the assimilation cycles.

400 Overall, errors in the maximum surface wind (MSW) and MSLP are greatly reduced after
401 assimilating radar data in all DA experiments. At 0300 UTC 13 September, the end of the DA
402 cycles, the best track MSW and MSLP are 47.5 m s^{-1} and 951 hPa respectively. For 3DVARb,
403 HybridF, and HybridH, after assimilating radar radial wind, the MSW errors are 1, 0.8, and 2.7
404 m s^{-1} and the MSLP errors are 0.2, 1.9, and 5.6 hPa, respectively. The larger MSW (which is not
405 directly observed) error in HybridH suggests that there is over-fitting of the analyzed wind to Vr
406 observations (Fig. 8a). For NoDA experiment without assimilating radar data, the MSW error is
407 9 m s^{-1} and MSLP error is 29 hPa.

408 *e. The analyzed hurricane structures*

409 We examine next the structure of the hurricane at the end of the DA cycles by plotting
410 fields at the surface and in vertical cross sections through the analyzed hurricane center. Figure 9
411 shows the analyzed mean sea level pressure and surface wind vectors for NoDA, 3DVARb,
412 HybridF and HybridH. Compared with NoDA (Fig. 9a), the analyzed vortex circulations are
413 stronger and the minimum sea level pressure is much lower in 3DVARb, HybridF, and HybridH

414 (Fig. 9b-d). Such primary hurricane circulations (Willoughby 1990) are captured well by the
415 assimilation of radar radial velocity data.

416 Figure 10 shows the vertical cross sections of horizontal wind speed and potential
417 temperature for all four experiments. The locations of cross sections are through the analyzed
418 hurricane center and the location of maximum wind speed of each experiment as indicated by the
419 thick lines in Fig. 9; the locations of MSLP and maximum wind for the four experiments are
420 slightly different. In NoDA, the hurricane eye is much wider and the intensity is much weaker
421 than in the three radar DA experiments. Unlike the hybrid experiments, the potential temperature
422 contours of 3DVARb (Fig. 10b) do not bend downward below ~600 hPa. The downward
423 extrusion of potential temperature contours in HybridF and HybridH indicates a warm core
424 structure (Fig. 10c, d). In experiment 3DVARb (Fig. 10b), the maximum wind speed at ~850 hPa
425 on the right side of eye wall is about 10 m s^{-1} larger than those in HybridF and HybridH (Fig. 10c,
426 d), but this larger wind speed is not accompanied by a warmer core expected of a stronger TC;
427 this is an indication that the 3DVAR analysis is not dynamically and thermodynamically
428 balanced.

429 Given the inner eye pressure deficit, the warm core should extend through the depth of
430 the troposphere based on the hydrostatic approximation (Haurwitz 1935). The warm core
431 structure is seen clearly in the vertical cross sections of horizontal temperature anomaly, which is
432 the deviation from the mean at the pressure levels (Fig. 11). The temperature anomaly in NoDA
433 is very small (less than 2 K, Fig. 11a) while that in 3DVARb, HybridF and HybridH exceeds 8 K,
434 with the maximum anomaly found between 300 and 500 hPa levels (Fig. 11b-d). This result is
435 consistent with observational studies; the strength of hurricane warm core has been shown to
436 negatively correlate with MSLP (Halverson et al. 2006; Hawkins and Imbembo 1976).

437 The near-zero or negative temperature anomaly below 700 hPa is clear in Fig. 11b for
438 3DVARb. This is related to the negative 3DVARb temperature increment discussed earlier. It is
439 worth noting that the 3DVARb analysis does produce a reasonable warm core aloft. In HybridF
440 and HybridH, the positive anomaly extends to the surface (Fig. 11c and 11d). In the latter two,
441 the maximum anomaly is found to be at the inner edge of hurricane eye wall at about 400 hPa,
442 which should be associated with the eye wall warming (LaSeur and Hawkins 1963; Holland
443 1997).

444 *f. The track and intensity forecasts*

445 To further evaluate the quality of analyses produced by different DA methods,
446 deterministic forecasts initialized from the (ensemble mean in the hybrid cases) analyses at 0300
447 UTC 13 September, the end of the DA cycles, are launched. The track forecasts are compared in
448 Figure 12a. The center of hurricane is defined as the location of MSLP. The initial track errors at
449 0300 UTC are less than 20 km for all four experiments. By 0000 UTC 14 September, the track
450 errors are 98, 117, 84, 64 km for NoDA, 3DVARb, HybridF and HybridH respectively. The
451 mean track errors based on the hurricane positions at 6-h interval during the period from 0300
452 UTC 13 to 0000 UTC 14 September are 41, 57, 41, and 34 km for NoDA, 3DVARb, HybridF,
453 and HybridH respectively. Given that our DA experiments do not include environmental
454 observations, the main effect on the track should come from the changes to the structure and
455 intensity of the analyzed hurricane.

456 Figure 12b shows the intensity forecasts in terms of MSLP, together with the best track
457 MSLP. At 0300 UTC 13 September, the MSLP errors are 28, 0.2, 2.0, and 5.5 hPa for NoDA,
458 3DVARb, HybridF and HybridH respectively. NoDA has the largest MSLP error throughout the
459 forecast. The MSLP error in 3DVARb is smaller at the initial time, but becomes larger than those

460 of HybridF and HybridH at the later forecast times. Overall, the forecast MSLP in the two hybrid
461 experiments is closer to the best track MSLP than that of 3DVARb. None of the forecasts
462 capture the slight deepening during the first 3 hours of forecast.

463 *g. Verification of forecasts against Vr observations*

464 The wind forecasts are further verified against observed radar radial velocity data. Figure
465 13 shows the root mean squared errors (RMSEs, strictly it is RMSD because observations also
466 contain error) of forecast against observed Vr for 3DVARb, HybridF and HybridH. Compared to
467 the best track estimation of wind speed, the radar Vr observations are more reliable. At the initial
468 time of 0300 UTC, the RMSE of 3.5 m s^{-1} from HybridF is slightly larger than those from
469 HybridH (2.6 m s^{-1}) and 3DVARb (2.8 m s^{-1}). After the first hour, the HybridF wind forecast fits
470 the observed radial wind best, especially after 6 hours of forecast where the error in 3DVARb
471 grows much faster and reaching 14.8 m s^{-1} compared to the $8\text{-}9 \text{ m s}^{-1}$ in the hybrid cases. The
472 much faster error growth in 3DVARb, even though its fit to Vr observations at the start of free
473 forecast is comparable to that of HybridH and better than HybridF, again suggests that other
474 model fields in the 3DVARb analysis are dynamically less consistent with the wind field than in
475 the hybrid cases. As shown in Fig. 7, major differences exist between the 3DVAR and hybrid
476 methods with the cross variable updating. This is further confirmed with the performance of
477 HybridH in Fig. 13. Even though the HybridH analysis is even more over-fitting to observations
478 than the 3DVAR (Fig. 8a), the forecast of HybridH was better than the 3DVAR due to the use of
479 ensemble covariance. Interestingly, this over-fitting to conventional temperature and wind
480 observations in 3DVAR analysis and worse fitting to observations in the forecast, compared with
481 Hybrid where the forecast ensemble perturbations were used to estimate background error
482 covariance, is also seen in other studies with quite different application (Fig. 2 of Wang et al.

483 2008b). The slight better forecast in HybridF than in HybridH at 6 hours suggests the fully flow-
484 dependent covariance during the assimilation cycles is beneficial.

485 *h. Evaluation of rainfall forecasts*

486 Rainfall forecasts are evaluated by calculating equitable threat scores (ETSs) of 3-h
487 accumulated precipitation against NCEP Stage IV precipitation analyses (Fig. 14). For the
488 thresholds of 5, 10, and 25 mm/3 hr and all forecast lead times, the hybrid experiments have
489 higher ETSs than 3DVARb. Furthermore, the improvement of the hybrid over 3DVARb
490 increases with precipitation threshold, indicating again the superior quality of the hybrid DA
491 method. In addition, HybridF has slightly higher ETS scores than HybridH for most times and
492 thresholds. The ETS of the hybrid experiments is higher than the NoDA for larger threshold and
493 longer forecast lead times. By further looking at the precipitation patterns, it is found that the
494 precipitation forecasts of HybridF more closely match the observed convective spiral band
495 patterns in the inner core region while 3DVARb produces too much precipitation in the southeast
496 quadrant in the outer band region (the region is within the reflectivity coverage of coastal radars,
497 from which the Stage IV precipitation is estimated, c.f. Fig. 1) and the radius of the inner core
498 eye wall appears larger than observed (Fig. 15). In comparison, the precipitation pattern from
499 NoDA case is poorer than the DA experiments especially for inner rain bands. We do note that
500 during the earlier hours and for lower thresholds, the ETSs of NoDA are comparable to those of
501 hybrid schemes and higher than those of 3DVARb. The exact cause is difficult to ascertain.
502 Imbalances and adjustments in the 3DVAR analyses with short analysis-forecast cycles might
503 have been a cause for the poorer performance but this is only a hypothesis.

504 **5. Summary and conclusions**

505 In this study, the WRF hybrid ensemble-3DVAR data assimilation (DA) system is
506 applied for the first time to the assimilation of radial velocity data for a landfalling hurricane.
507 More specifically, radial velocity data from two operational WSR-88D radars along the Gulf of
508 Mexico coast are assimilated over a three-hour period after Hurricane Ike (2008) moved into the
509 coverage of the two radars, using an enhanced version of the WRF hybrid DA system. Instead of
510 using an ensemble transformation Kalman filter as in an earlier study to generate the analysis
511 ensemble, we employ in this study the ‘perturbed observation’ method. Further, we applied
512 vertical localization based on empirical orthogonal functions while continuing to use recursive
513 filters for horizontal localization for the flow-dependent ensemble-estimated background error
514 covariance. The flow-dependent ensemble covariance is incorporated into the 3D variational
515 framework by using the extended control variable method.

516 The radial velocity data are assimilated every 30 minutes over a 3 hour period. Results
517 mainly from five experiments are presented. A forecast experiment without assimilating any
518 radar data is first carried out to serve as a baseline against which the radar-assimilating
519 experiments are compared; this forecast experiment (NoDA) started directly from the operational
520 GFS analysis, which contained too weak a hurricane vortex. The four radar DA experiments
521 used the WRF 3DVAR using the static covariance derived from the NMC method (3DVARa),
522 the WRF 3DVAR using further tuned static covariance (3DVARb), the hybrid DA system with
523 purely flow-dependent background covariance (HybridF), as well as half static and half flow-
524 dependent covariance (HybridH), respectively. In the tuned 3DVAR experiment (3DVARb) as
525 well as HybridH, the horizontal spatial correlation scale in the static covariance derived from the
526 NMC-method is reduced by a factor of 0.3 to produce much more realistic wind increments than

527 the default scale (in 3DVARa). The results of analyses and forecasts from the five experiments
528 are inter-compared and verified against best track data, radar wind measurements, and
529 precipitation data. The main conclusions are summarized in the following.

530 (1) HybridF produces the most realistic temperature increments with positive values at
531 the hurricane center, corresponding to the warm core structure, while 3DVARb produces much
532 weaker and smoother temperature increments that are negative at the center of hurricane. At the
533 end of assimilation cycles, negative temperature anomalies are found at lower levels in the eye
534 region of 3DVARb analysis while the hybrid analyses show deep warm core structures.

535 (2) All three DA experiments are able to create analyses that fit the Vr data well, and the
536 error reduction by analysis is the largest in the first analysis cycle. Most of the minimum sea
537 level pressure (MSLP) reduction is achieved through model adjustment during the forecast step
538 of the assimilation cycles

539 (3) The hybrid experiments improve the Ike track forecast slightly, over the track forecast
540 by NoDA starting from the GFS analysis. 3DVARb slightly degrades the track forecast. All radar
541 DA experiments produce MSLP forecasts closer to the best track observation than NoDA does.

542 (4) The fit of forecast radial velocity to radar observations of 3DVARb is much worse
543 than those of HybridF and HybridH. The forecast results indicate that the overall quality of
544 hybrid analyses is better than that of 3DVARb, producing more dynamically consistent state
545 estimations that lead to later slower error growth during forecast. The forecast error of HybridF
546 is slightly lower than that of HybridH starting from hour three.

547 (5) The equitable threat scores (ETSs) for 3-hour accumulated precipitation forecasts in
548 the hybrid experiments are higher than those of 3DVARb for the thresholds and lead times
549 considered, and the improvement increases with precipitation threshold, indicating again the

550 superior quality of the hybrid DA method. Among the hybrid experiments, HybridF produced
551 slightly better ETSs than HybridH at most verification times.

552 (6) The results of this study also show positive impacts of assimilating radar data for
553 hurricane initialization, and the hybrid-method-analyzed hurricane has kinematic and
554 thermodynamic structures that are consistent with tropical cyclone conceptual models.

555 Finally a point worth noting: the inclusion of static background covariance in HybridH
556 in general did not improve the results over HybridF in this case study; i.e., the use of flow-
557 dependent covariance in full in general gives better results. Earlier studies (Hamill and Snyder
558 2000; Wang et al. 2007a) suggested that the optimal combination of the static and flow-
559 dependent covariance depends on their relative quality. The results in this case study suggest that
560 for hurricanes and radar data, there is likely little benefit of including static covariance because if
561 the static covariance is not capable of appropriately reflecting the mesoscale and convective-
562 scale nature of hurricanes.

563 We also note that this study represents the first attempt of applying a variational-
564 ensemble hybrid data assimilation method to hurricane and radar data assimilation. While the
565 results are positive and encouraging, more robust conclusions will need to be drawn by testing
566 the method on many more cases.

567

568 *Acknowledgements:* This research was primarily supported by a subcontract to a grant from the
569 Mississippi State University led by Dr. Haldun Karan. The first author also acknowledges Dr.
570 Curtis N. James for radar data processing, Shizhang Wang, Alex Schenkman, and Dr. Robin
571 Tanamachi for helpful discussions and assistance with initial drafts. This work was also
572 supported by NSF grant AGS-0802888, DOD-ONR grant N00014-10-1-0775, NOAA

573 THOPREX grant NA08OAR4320904, NASA NIP grant NNX10AQ78G and NOAA HFIP grant
574 NA12NWS4680012. The experiments were conducted on a supercomputer at the Mississippi
575 State University.
576

577 **References**

- 578 Aksoy, A., S. Lorusso, T. Vukicevic, K. J. Sellwood, S. D. Aberson and F. Zhang, 2012: The
579 HWRF Hurricane Ensemble Data Assimilation System (HEDAS) for high-resolution data:
580 The impact of airborne Doppler radar observations in an OSSE. *Mon. Wea. Rev.*, in
581 press.
- 582 Barker, D. M., W. Huang, Y. R. Guo, A. J. Bourgeois, and Q. N. Xiao, 2004: A Three-
583 Dimensional Variational Data Assimilation System for MM5: Implementation and Initial
584 Results. *Mon. Wea. Rev.* , 132, 897-914.
- 585 Buehner, M., 2005: Ensemble-derived stationary and flow-dependent background-error
586 covariances: Evaluation in a quasi-operational NWP setting. *Quart. J. Roy. Meteor. Soc.*,
587 131, 1013-1043.
- 588 ---, P. L. Houtekamer, C. Charette, H. L. Mitchell, and B. He, 2010a: Intercomparison of
589 variational data assimilation and the ensemble Kalman filter for global deterministic
590 NWP. Part I: Description and single-observation experiments. *Mon. Wea. Rev.*, 138,
591 1550-1566.
- 592 ---,--,--,--, and --, 2010b: Intercomparison of variational data assimilation and the ensemble
593 Kalman filter for global deterministic NWP. Part II: One-month experiments with real
594 observations. *Mon. Wea. Rev.*, 138, 1567-1586.
- 595 Burgers, G., P. J. van Leeuwen, and G. Evensen, 1998: Analysis scheme in the ensemble Kalman
596 filter, *Mon. Wea. Rev.*, 126, 1719--1724.
- 597 Dong, J., and M. Xue, 2012: Coastal WSR-88D Radar Data Assimilation with Ensemble Kalman
598 Filter for Analysis and Forecast of Hurricane Ike (2008). *Quart. J. Roy. Meteor. Soc.*,
599 Accepted.

600 Dowell, D. C. and L. J. Wicker, 2009: Additive Noise for Storm-Scale Ensemble Data
601 Assimilation. *J. Atmos Ocean Tech*, 26, 911-927.

602 Dudhia, J., 1989: Numerical study of convection observed during the Winter Monsoon
603 Experiment using a mesoscale two-dimensional model. *J. Atmos. Sci.*, 46, 3077-3107.

604 Etherton, B. J., and C. H. Bishop, 2004: The resilience of hybrid ensemble/3D-Var analysis
605 schemes to model error and ensemble covariance error. *Mon. Wea. Rev.*, 132, 1065-1080.

606 Evensen, G., 2003: The ensemble Kalman filter: Theoretical formulation and practical
607 implementation. *Ocean Dynamics*, 53, 343-367.

608 Grell, G. A. and D. Devenyi, 2002: A generalized approach to parameterizing convection
609 combining ensemble and data assimilation techniques. *Geophys Res Lett*, 29(14), Article
610 1693.

611 Halverson, J. B., J. Simpson, G. Heymsfield, H. Pierce, T. Hock, and L. Ritchie, 2006: Warm
612 core structure of Hurricane Erin diagnosed from high altitude dropsondes during
613 CAMEX-4. *J Atmos Sci*, 63, 309-324.

614 Hamill, T. M. and C. Snyder, 2000: A hybrid ensemble Kalman filter-3D variational analysis
615 scheme. *Mon. Wea. Rev.*, 128, 2905-2919.

616 Hamill, T. M., J. S. Whitaker, M. Fiorino, and S. G. Benjamin, 2011: Global ensemble
617 predictions of 2009's tropical cyclones initialized with an ensemble Kalman filter. *Mon.*
618 *Wea. Rev.*, 139, 668-688.

619 Haurwitz, B., 1935: The height of tropical cyclones and the eye of the storm. *Mon. Wea. Rev.*, 63,
620 45-49.

621 Hawkins, H. F. and S. M. Imbembo, 1976: The structure of a small, intense hurricane-Inez 1966.
622 *Mon. Wea. Rev.*, 104, 418-442.

623 Holland, G. J., 1997: The maximum potential intensity of tropical cyclones. *J. Atmos. Sci.*, 54,
624 2519-2541.

625 Hong, S.-Y., J. Dudhia, and S.-H. Chen, 2004: A revised approach to ice microphysical
626 processes for the bulk parameterization of clouds and precipitation. *Monthly Weather*
627 *Review*, 132, 103-120.

628 Houtekamer, P. L., and H. L. Mitchell, 1998: Data Assimilation Using an Ensemble Kalman
629 Filter Technique. *Mon. Wea. Rev.*, 126, 796–811.

630 Hu, M., M. Xue, J. Gao, and K. Brewster, 2006: 3DVAR and cloud analysis with WSR-88D
631 level-II data for the prediction of Fort Worth tornadic thunderstorms. Part II: Impact of
632 radial velocity analysis via 3DVAR. *Mon. Wea. Rev.*, 134, 699-721.

633 James, C. N. and R. A. Houze, 2001: A real-time four-dimensional Doppler dealiasing scheme. *J*
634 *Atmos Ocean Tech*, 18, 1674-1683.

635 Kleist, D., K. Ide, J. Whitaker, J. C. Derber, D. Parrish and X. Wang, 2011: Expanding the GSI
636 based hybrid ensemble-variational system to include more flexible parameter settings.
637 Paper J16.4. AMS Annual meeting, Seattle, WA. Jan. 23-27, 2011

638 Kurihara, Y., M. A. Bender, R. E. Tuleya, and R. Ross, 1995: Improvements in the GFDL
639 hurricane prediction system. *Mon. Wea. Rev.*, 123, 2791-2801.

640 La Seur, N. E., and H. F. Hawkins, 1963: An analysis of Hurricane Cleo (1958) based on data
641 from research reconnaissance aircraft. *Mon. Wea. Rev.*, 91, 694-709.

642 Liu, C., Q. Xiao, and B. Wang, 2008: An ensemble-based four-dimensional variational data
643 assimilation scheme. Part I: Technical formulation and preliminary test. *Mon. Wea. Rev.*,
644 136, 3363–3373.

645 ———, ———, and ———, 2009: An ensemble-based four-dimensional variational data assimilation

646 scheme. Part II: Observing System Simulation Experiments with Advanced Research
647 WRF (ARW). *Mon. Wea. Rev.*, 137, 1687–1704.

648 Li, J., and H. Liu, 2009: Improved hurricane track and intensity forecast using singlefield-of-
649 view advanced IR sounding measurements. *Geophys. Res. Lett.*, 36, L11813.

650 Liu, Q., T. Marchok, H.-L. Pan, M. Bender, and S. J. Lord, 2000: Improvements in hurricane 2
651 initialization and forecasting at NCEP with global and regional (GFDL) models. Tech.
652 rep., 3 NOAA Tech. Procedures Bull. 472, 7 pp., Camp Springs, MD.

653 Liu, S., M. Xue, J. Gao, and D. Parrish, 2005: Analysis and impact of super-obbed Doppler
654 radial velocity in the NCEP grid-point statistical interpolation (GSI) analysis system.
655 *Extended abstract, 17th Conf. Num. Wea. Pred.*, Washington DC, Amer. Meteor. Soc.,
656 13A.4.

657 Lorenc, A., 2003: The potential of the ensemble Kalman filter for NWP - a comparison with 4D-
658 Var. *Quart. J. Roy. Meteor. Soc.*, 129, 3183-3204.

659 Mlawer, E. J., S. J. Taubman, P. D. Brown, M. J. Iacono, and S. A. Clough, 1997: Radiative
660 transfer for inhomogeneous atmospheres: RRTM, a validated correlated-k model for the
661 longwave. *J. Geophys. Res.*, 102, 16663-16682.

662 Noh, Y., W. G. Cheon, S. Y. Hong, and S. Raasch, 2003: Improvement of the K-profile model
663 for the planetary boundary layer based on large eddy simulation data. *Bound-Lay*
664 *Meteorol*, 107, 401-427.

665 Parrish, D. F. and J. C. Derber, 1992: The National Meteorological Center's spectral statistical-
666 interpolation analysis system. *Mon. Wea. Rev.*, 120, 1747-1763.

667 Pielke, R. A., J. Gratz, C. W. Landsea, D. Collins, M. A. Saunders, and R. Musulin, 2008:
668 Normalized hurricane damage in the United States: 1900-2005. *Natural hazards Review*,

669 29-42.

670 Schenkman, A., M. Xue, A. Shapiro, K. Brewster, and J. Gao, 2011: The analysis and prediction
671 of the 8-9 May 2007 Oklahoma tornadic mesoscale convective system by assimilating
672 WSR-88D and CASA radar data using 3DVAR. *Mon. Wea. Rev.*, 139, 224-246.

673 Skamarock, W. C., J. B. Klemp, J. Dudhia, D. O. Gill, D. M. Barker, M. Duda, X.-Y. Huang, W.
674 Wang and J. G. Powers, 2008: A Description of the Advanced Research WRF Version 3.
675 NCAR Technical Note TN-475+STR, 113 pp .

676 Torn, R. D., and G. J. Hakim, 2009: Initial condition sensitivity of western-Pacific extratropical
677 transitions determined using ensemble-based sensitivity analysis. *Mon. Wea. Rev.* 137,
678 3388-3406.

679 ---, ---, and C. Snyder, 2006: Boundary conditions for limited-area ensemble Kalman filters. *Mon.*
680 *Wea. Rev.*, 134, 2490–2502.

681 Wang, X., T. M. Hamill, J. S. Whitaker and C. H. Bishop, 2007a: A comparison of hybrid
682 ensemble transform Kalman filter-OI and ensemble square-root filter analysis schemes.
683 *Mon. Wea. Rev.*, 135, 1055-1076.

684 ---, C. Snyder, and T. M. Hamill, 2007b: On the theoretical equivalence of differently proposed
685 ensemble/3D-Var hybrid analysis schemes. *Mon. Wea. Rev.*, 135, 222-227.

686 ---, D. M. Barker, C. Snyder, and T. M. Hamill, 2008a: A Hybrid ETKF-3DVAR Data
687 Assimilation Scheme for the WRF Model. Part I: Observing system simulation
688 experiment. *Mon. Wea. Rev.*, 136, 5116-5131.

689 ---, ---, ---, and ---, 2008b: A hybrid ETKF-3DVAR data assimilation scheme for the WRF model.
690 Part II: Real observation experiment. *Mon. Wea. Rev.*, 136, 5132-5147.

691 ---, T. M. Hamill, J. S. Whitaker, C. H. Bishop, 2009: A comparison of the hybrid and EnSRF

692 analysis schemes in the presence of model error due to unresolved scales. *Mon. Wea. Rev.*,
693 137,3219-3232

694 ---, 2010: Incorporating ensemble covariance in the Gridpoint Statistical Interpolation (GSI)
695 variational minimization: a mathematical framework. *Mon. Wea. Rev.*, 138,2990-2995.

696 ---, 2011: Application of the WRF hybrid ETKF-3DVAR data assimilation system for hurricane
697 track forecasts. *Wea. Forecasting*, 26, 868-884.

698 ----, T. Lei, J. Whitaker, D. Parrish, and D. Kleist, 2011: GSI-based hybrid ensemble-variational
699 data assimilation system for the Global Forecast system model: 3DVAR-based hybrid
700 and ensemble 4DVAR. Paper J16.5. AMS Annual meeting, Seattle, WA. Jan. 23-27,
701 2011.

702 ----, D. Parrish, D. Kleist, and J. Whitaker, 2012: GSI-based hybrid variational-EnKF data
703 assimilation for NCEP Global Forecast System: single resolution experiments., *Mon.*
704 *Wea. Rev.*, submitted.

705 Weng, Y., M. Zhang, and F. Zhang, 2011: Advanced data assimilation for cloud-resolving
706 hurricane initialization and prediction. *Comput. Sci. Eng.*, 13, 40-49.

707 Weng, Y. and F. Zhang, 2012: Assimilating Airborne Doppler Radar Observations with an
708 Ensemble Kalman Filter for Convection-Permitting Hurricane Initialization and
709 Prediction: Katrina (2005). *Mon. Wea. Rev.*, 140, 841-859.

710 Whitaker, J., D. Kleist, X. Wang and T. Hamill, 2011: Tests of a hybrid variational-ensemble
711 global assimilation system for hurricane prediction. Paper J16.2. AMS annual meeting,
712 2011, Seattle, WA.

713 Willoughby, H. E., 1990: Temporal changes in the primary circulation in tropical cyclones. *J.*
714 *Atmos. Sci.*, 47, 242–264.

715 Sugimoto, S., N. A. Crook, J. Sun, Q. Xiao, and D. Barker, 2009: Assimilation of Doppler
716 Radar Data with WRF 3DVAR: Evaluation of its Potential Benefits to Quantitative
717 Precipitation Forecasting through Observing System Simulation Experiments. *Mon. Wea.*
718 *Rev.*, **137**, 4011-4029.

719 Xiao, Q. N., and J. Sun, 2007: Multiple radar data assimilation and short-range quantitative
720 precipitation forecasting of a squall line observed during IHOP_2002. *Mon. Wea. Rev.*,
721 **135**, 3381-3404.

722 ---, X. Y. Zhang, C. Davis, J. Tuttle, G. Holland, and P. J. Fitzpatrick, 2009: Experiments of
723 Hurricane Initialization with Airborne Doppler Radar Data for the Advanced Research
724 Hurricane WRF (AHW) Model. *Mon Weather Rev*, **137**, 2758-2777.

725 Xu, Q. and J. D. Gong, 2003: Background error covariance functions for Doppler radial-wind
726 analysis. *Q J Roy Meteor Soc*, **129**, 1703-1720.

727 Zhang, F., C. Snyder, and J. Sun, 2004: Impacts of initial estimate and observations on the
728 convective-scale data assimilation with an ensemble Kalman filter. *Mon. Wea. Rev.*, **132**,
729 1238-1253.

730 Zhang, F., Y. Weng, J. A. Sippel, Z. Meng, and C. H. Bishop, 2009: Cloud-resolving hurricane
731 initialization and prediction through assimilation of Doppler radar observations with an
732 ensemble Kalman filter. *Mon. Wea. Rev.*, **137**, 2105-2125.

733 Zhang, F., M. Zhang and J. A. Hansen, 2009: Coupling ensemble Kalman filter with four-
734 dimensional variational data assimilation. *Advances in Atmospheric Sciences* , **26**, 1-8.

735 Zhang, F., Y. Weng, J. F. Gamache, and F. D. Marks, 2011: Performance of convection-
736 permitting hurricane initialization and prediction during 2008-2010 with ensemble data
737 assimilation of inner-core airborne Doppler radar observations. *Geophys. Res. Lett.*, **38**,
738 L15810, doi:10.1029/2011GL048469.

739 Zhao, K. and M. Xue, 2009: Assimilation of coastal Doppler radar data with the ARPS 3DVAR
740 and cloud analysis for the prediction of Hurricane Ike (2008). *Geophys. Res. Lett.*, 36,
741 L12803.

742 Zou, X. L. and Q. N. Xiao, 2000: Studies on the initialization and simulation of a mature
743 hurricane using a variational bogus data assimilation scheme. *J. Atmos. Sci.*, 57, 836-860.

744 Zupanski, M., 2005: Maximum Likelihood Ensemble Filter: Theoretical Aspects. *Mon. Wea.*
745 *Rev.*, 133, 1710-1726.

746

747

748

749

750

751

752

753

754

755

756

757 **Figure Captions**

758 Fig. 1. The WRF model domain and National Hurricane Center best track positions for Hurricane
759 Ike (2008) from 1800 UTC 12 to 0000 UTC 14 September 2008. Also indicated are the
760 Houston, Texas (KHGX) and Lake Charles, Louisiana (KLCH) WSR-88D radar
761 locations (asterisks) and maximum range (300 km for radial velocity and 460 km for the
762 reflectivity) coverage circles.

763 Fig. 2. Schematic diagram of the hybrid ensemble-3DVAR forecast-analysis cycle for a
764 hypothetical three-member ensemble. Each member assimilates the observations
765 containing a different set of perturbations.

766 Fig. 3. The radial velocity (interval of 20 m s⁻¹) at 0.5° elevation angle from (a) KHGX and (b)
767 KLCH WSR-88D radars at 0000 UTC 13 September 2008. Black dot is for NHC best-
768 track position of Hurricane Ike (2008) at this time. Asterisks are for radar locations.

769 Fig. 4. The flow charts for (a) NoDA experiment, (b) 3DVAR experiments (3DVARa and
770 3DVARb), and (c) hybrid experiments (HybridF and HybridH).

771 Fig. 5. The vertical cross section of the wind speed increment (interval of 5 m s⁻¹) using a
772 single KHGX radar radial velocity data located at (28.4°N, 93.7°W, 3176 m) with an
773 innovation of -38.63 m s⁻¹ using the configurations of experiment HybridF but (a)
774 without and (b) with vertical localization at 0000 UTC 13 September 2008.

775 Fig. 6. The 700 hPa wind analysis increments (m s⁻¹) for (a) 3DVARa, (b) 3DVARb, (c)
776 HybridF, and (d) HybridH at 0000 UTC 13 September 2008.

777 Fig. 7. The 850 hPa temperature analysis increments for (a) 3DVARb (at intervals of 0.3 K),
778 (b) HybridF (at intervals of 0.7 K), and (c) HybridH (at intervals of 0.3 K), at 0000

779 UTC 13 September 2008.

780 Fig. 8. The forecast and analysis (sawtooth pattern during DA cycling) of (a) RMSD of radial
781 velocity (m s^{-1}), and (b) the minimum sea level pressures (hPa) together with the
782 NHC best track estimate, for 3DVARb, HybridF, and HybridH from 0000 to 0300
783 UTC 13 September 2008.

784 Fig. 9. The analyzed sea level pressure (interval of 5 hPa, solid contours) and the surface
785 wind vectors (m s^{-1}) for (a) NoDA, (b) 3DVARb, (c) HybridF, and (d) HybridH at
786 0300 UTC 13 September 2008. The thick solid line indicates the vertical cross section
787 location in Fig. 10 and Fig. 11.

788 Fig. 10. Vertical cross sections of analyzed horizontal wind speed (interval of 10 m s^{-1} ,
789 shaded) and potential temperature (interval of 5 K, solid contours) for (a) NoDA, (b)
790 3DVARb, (c) HybridF, and (d) HybridH, at 0300 UTC 13 September 2008.

791 Fig. 11. Vertical cross sections of analyzed temperature anomalies (interval of 2 K) for (a)
792 NoDA, (b) 3DVARb, (c) HybridF, and (d) HybridH, at 0300 UTC 13 September
793 2008.

794 Fig. 12. Deterministic forecast hurricane (a) tracks and (b) minimum sea level pressure (hPa)
795 by NoDA, 3DVARb, HybridF, and HybridH as compared to NHC best track
796 estimates from 0300 UTC 13 through 0000 UTC 14 September 2008.

797 Fig. 13. Deterministic forecast RMSEs of V_r (m s^{-1}) by 3DVARb, HybridF, and HybridH
798 from 0300 to 0900 UTC 13 September 2008.

799 Fig. 14. The equitable threat scores for 3 h accumulated forecast precipitation by NoDA,
800 3DVARb, HybridF, and HybridH at thresholds (a) 5 mm, (b) 10 mm, and (c) 25 mm,
801 verified against NCEP Stage-IV precipitation analyses valid at 0600, 0900, 1200, and

802 1500 UTC 13 September 2008.

803 Fig. 15 Three-hour accumulated precipitation (mm) by (1st column) NCEP Stage-IV
804 precipitation analyses, (2nd column) NoDA, (3rd column) 3DVARb, and (4th column)
805 HybridF valid at (top) 0600 and (bottom) 0900 UTC 13 September 2008.
806

807

Table 1. List of experiments

Experiment	Description
NoDA	No radar data assimilation. WRF model initial condition interpolated from NCEP 1°x1° analysis
3DVARa	Radar DA using WRF 3DVAR with static covariance from NMC method
3DVARb	Same as 3DVARa, except the horizontal spatial correlation in the static covariance is multiplied by 0.3.
HybridF	Radar DA using hybrid method with full weight given to flow dependent covariance, with $1/\beta_1 = 1/1001$ and $1/\beta_2 = 1/1.001$ in Eq. (1)
HybridH	Hybrid method with equal weight given to static covariance (which is the same as 3DVARb) and flow-dependent covariance, with $1/\beta_1 = 1/2$ and $1/\beta_2 = 1/2$ in Eq. (1)

808

809

810

811

812

813

814

815

816

817

818

819

820

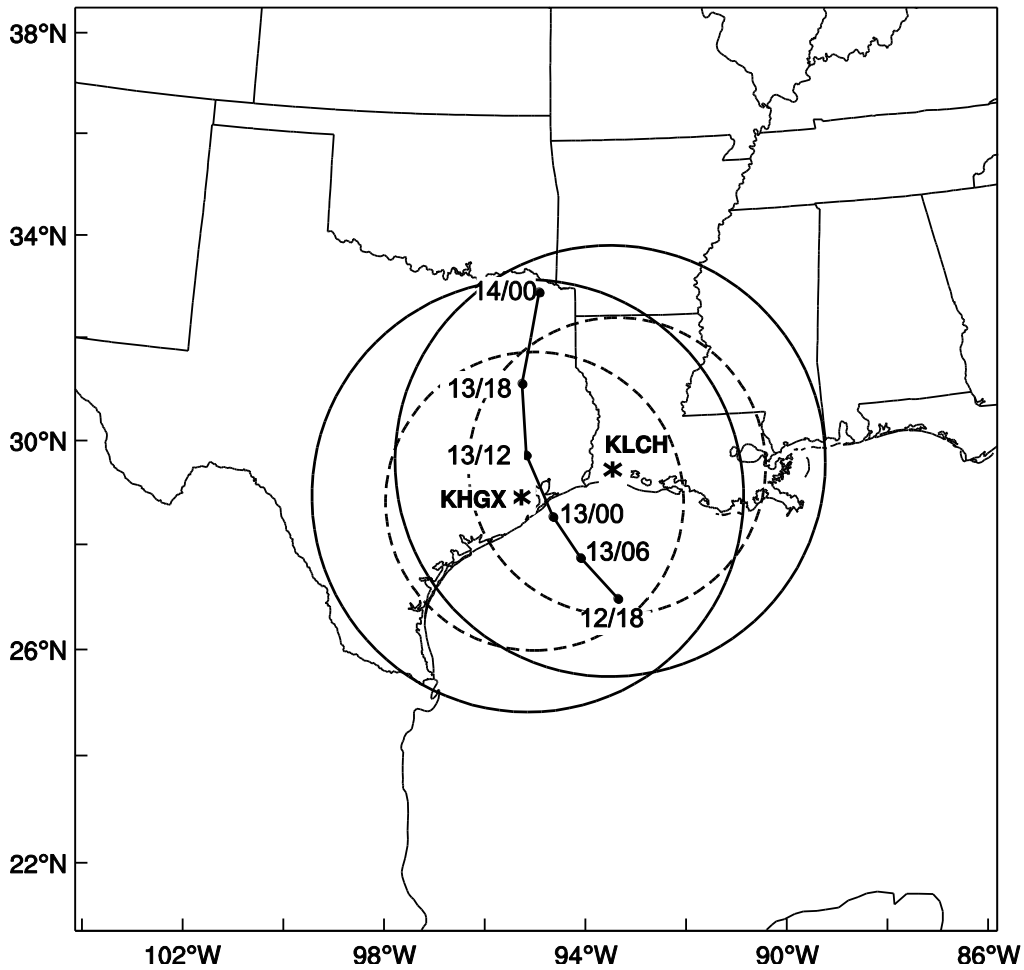
821

822

823

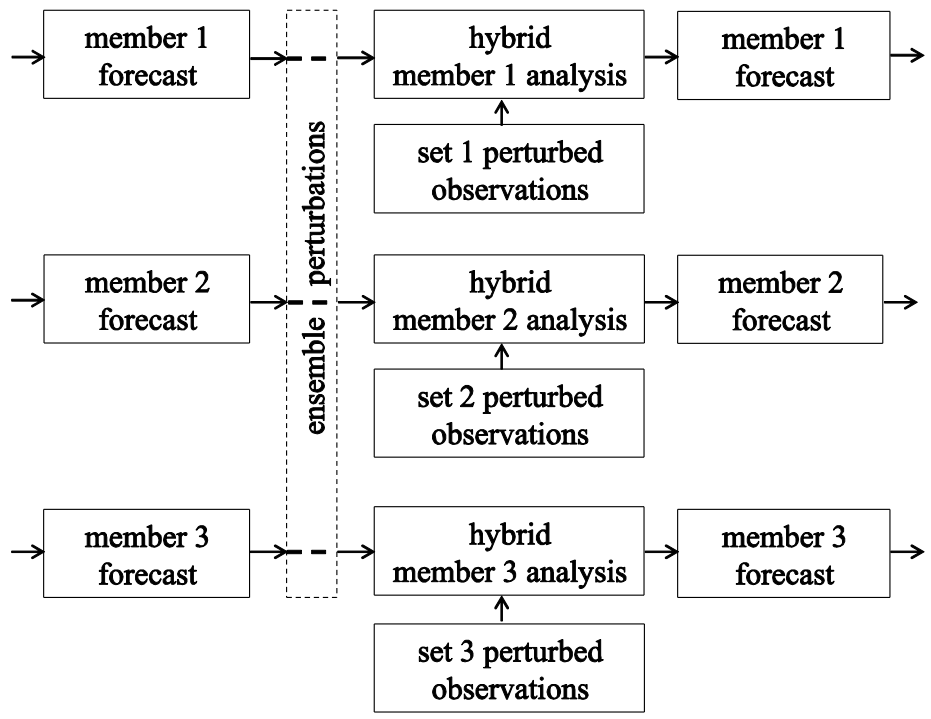
824

825



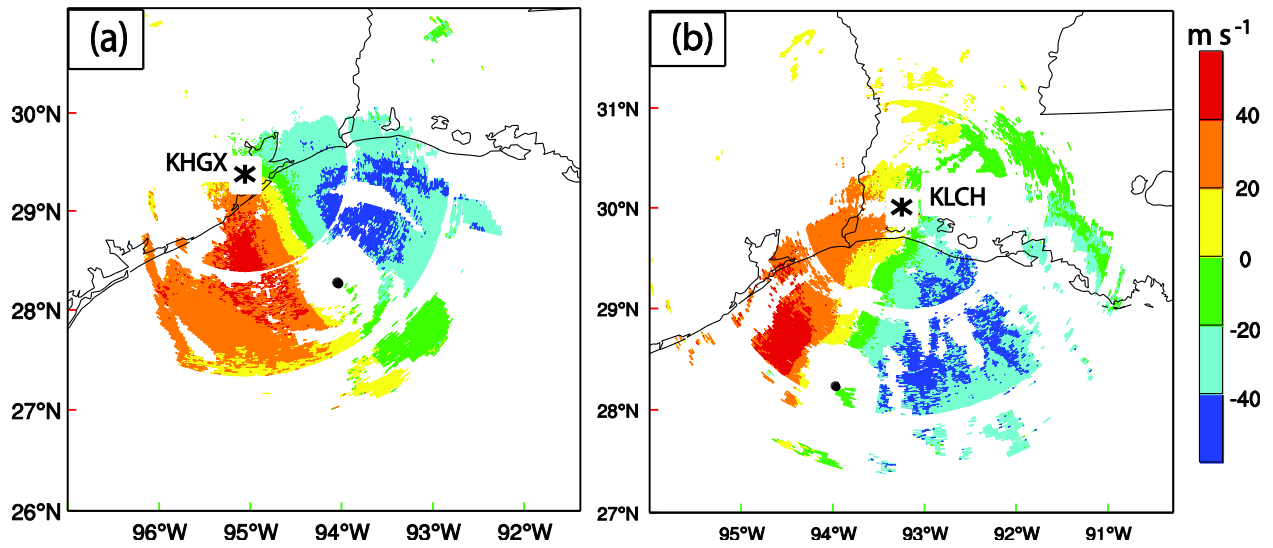
826
 827
 828
 829
 830
 831
 832
 833
 834
 835
 836
 837
 838
 839
 840
 841
 842

Fig. 1. The WRF model domain and National Hurricane Center best track positions for Hurricane Ike (2008) from 1800 UTC 12 to 0000 UTC 14 September 2008. Also indicated are the Houston, Texas (KHGX) and Lake Charles, Louisiana (KLCH) WSR-88D radar locations (asterisks) and maximum range (300 km for radial velocity and 460 km for the reflectivity) coverage circles.



843
 844
 845
 846
 847
 848
 849
 850
 851
 852
 853
 854
 855
 856
 857
 858
 859
 860

Fig. 2. Schematic diagram of the hybrid ensemble-3DVAR forecast-analysis cycle for a hypothetical three-member ensemble. Each member assimilates the observations containing a different set of perturbations.



861
862

863

864 Fig. 3. The radial velocity (interval of 20 m s^{-1}) at 0.5° elevation angle from (a) KHXG and (b)
865 KLCH WSR-88D radars at 0000 UTC 13 September 2008. Black dot is for NHC best-track
866 position of Hurricane Ike (2008) at this time. Asterisks are for radar locations.

867

868

869

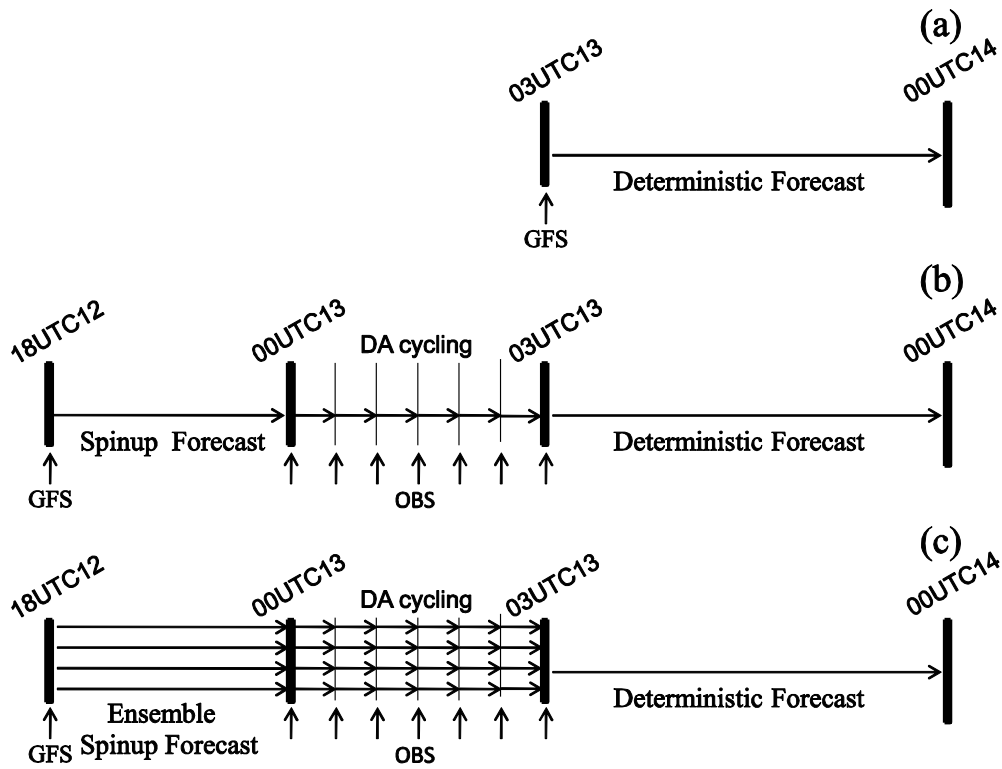
870

871

872

873

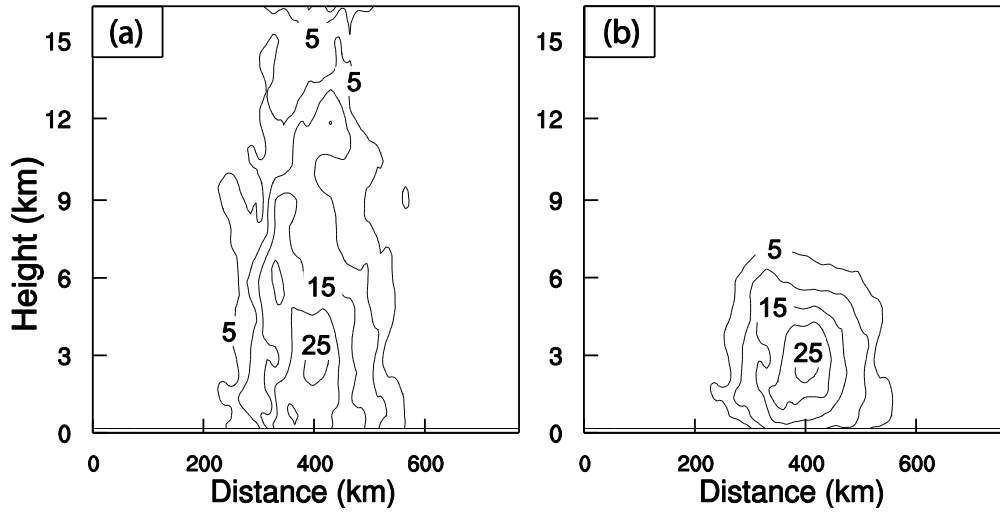
874



875
876
877

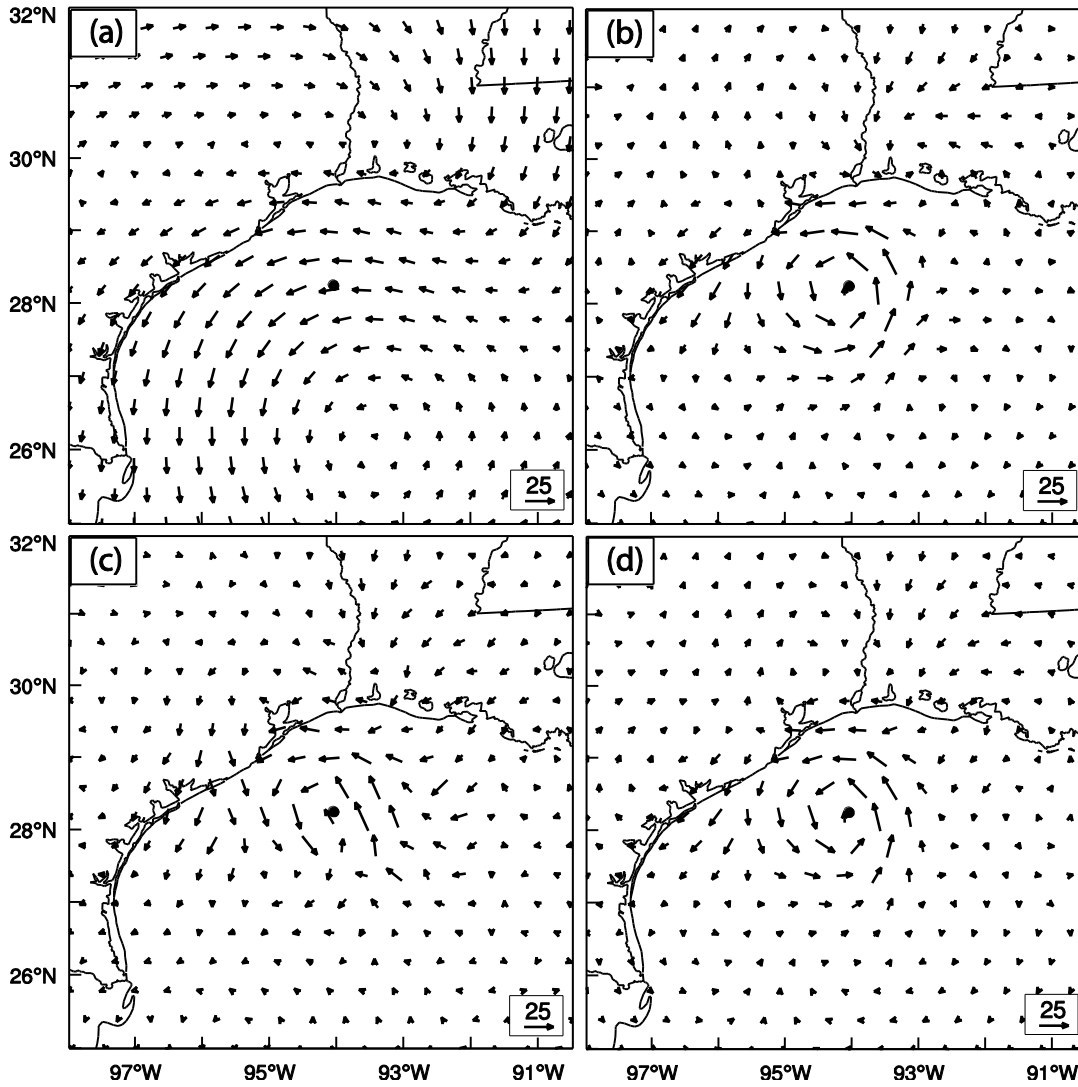
878 Fig. 4. The flow charts for (a) NoDA experiment, (b) 3DVAR experiments (3DVARa
879 and 3DVARb), and (b) hybrid experiments (HybridF and HybridH).
880

881
882
883
884
885
886
887
888
889
890
891
892



893
 894
 895
 896
 897
 898
 899
 900
 901
 902
 903
 904
 905
 906
 907
 908
 909
 910
 911
 912
 913
 914
 915
 916
 917

Fig. 5. The vertical cross section of the wind speed increment (interval of 5 m s^{-1}) using a single KHGX radar radial velocity data located at $(28.4^\circ\text{N}, 93.7^\circ\text{W}, 3176 \text{ m})$ with an innovation of -38.63 m s^{-1} using the configurations of experiment HybridF but (a) without and (b) with vertical localization at 0000 UTC 13 September 2008.



918

919

920 Fig. 6. The 700 hPa wind analysis increments (m s^{-1}) for (a) 3DVARa, (b) 3DVARb,
 921 (c) HybridF, and (d) HybridH at 0000 UTC 13 September 2008.

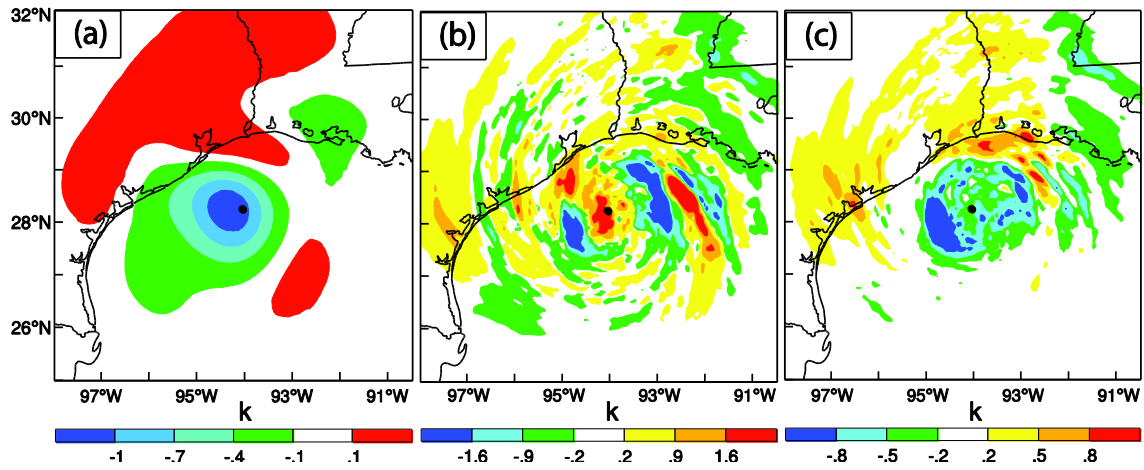
922

923

924

925

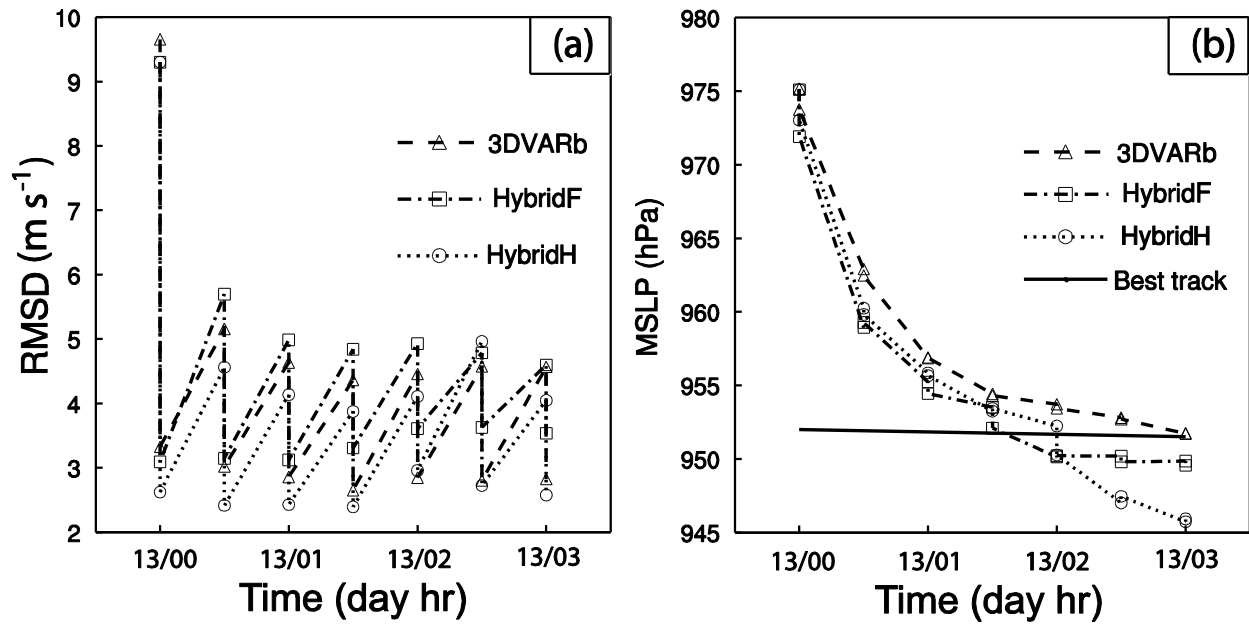
926



927
928

929 Fig. 7. The 850 hPa temperature analysis increments for (a) 3DVARb (at intervals of
930 0.3 K), (b) HybridF (at intervals of 0.7 K), and (c) HybridH (at intervals of 0.3 K), at
931 0000 UTC 13 September 2008.

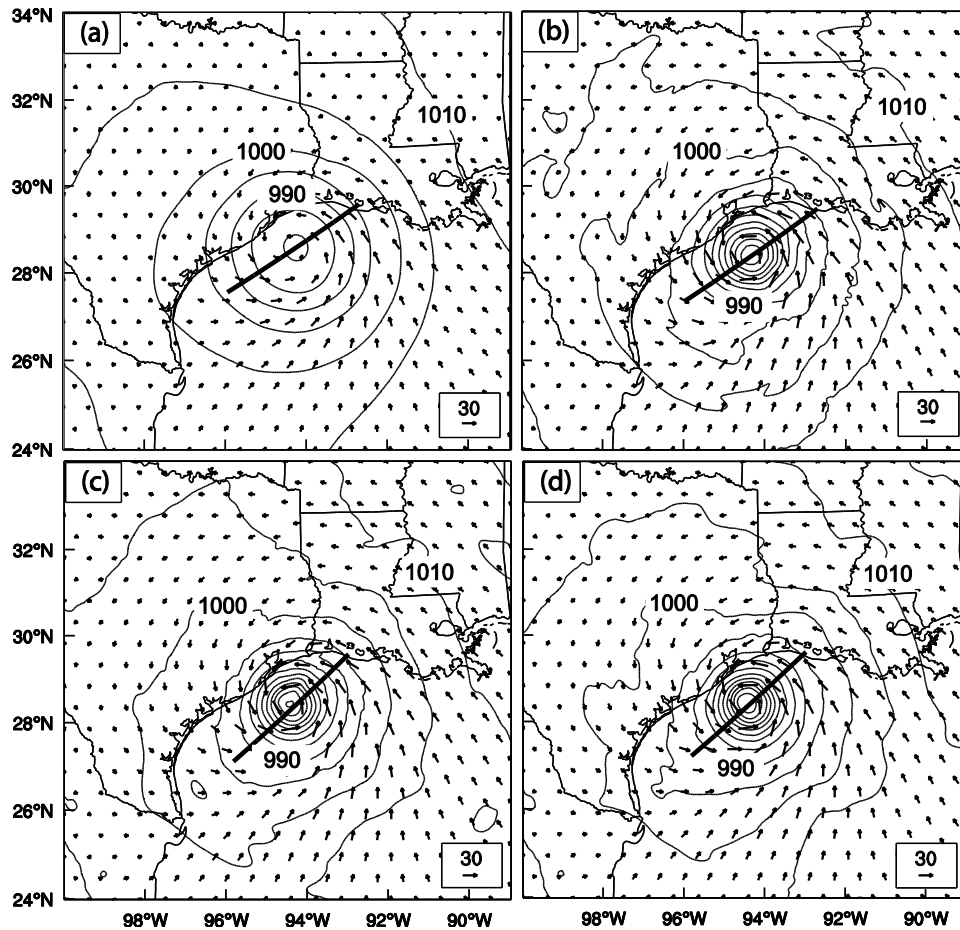
932
933
934
935
936
937
938
939
940
941
942
943
944
945
946
947
948
949
950



951
952

953 Fig. 8. The forecast and analysis (sawtooth pattern during DA cycling) of (a) RMSD
954 of radial velocity (m s^{-1}), and (b) the minimum sea level pressures (hPa) together with
955 the NHC best track estimate, for 3DVARb, HybridF, and HybridH from 0000 to 0300
956 UTC 13 September 2008.

957
958
959
960
961
962
963
964
965
966
967
968
969
970
971



972

973

974

975 Fig. 9. The analyzed sea level pressure (interval of 5 hPa, solid contours) and the
 976 surface wind vectors (m s^{-1}) for (a) NoDA, (b) 3DVARb, (c) HybridF, and (d)
 977 HybridH at 0300 UTC 13 September 2008. The thick solid line indicates the vertical
 978 cross section location in Fig. 10 and Fig. 11.

979

980

981

982

983

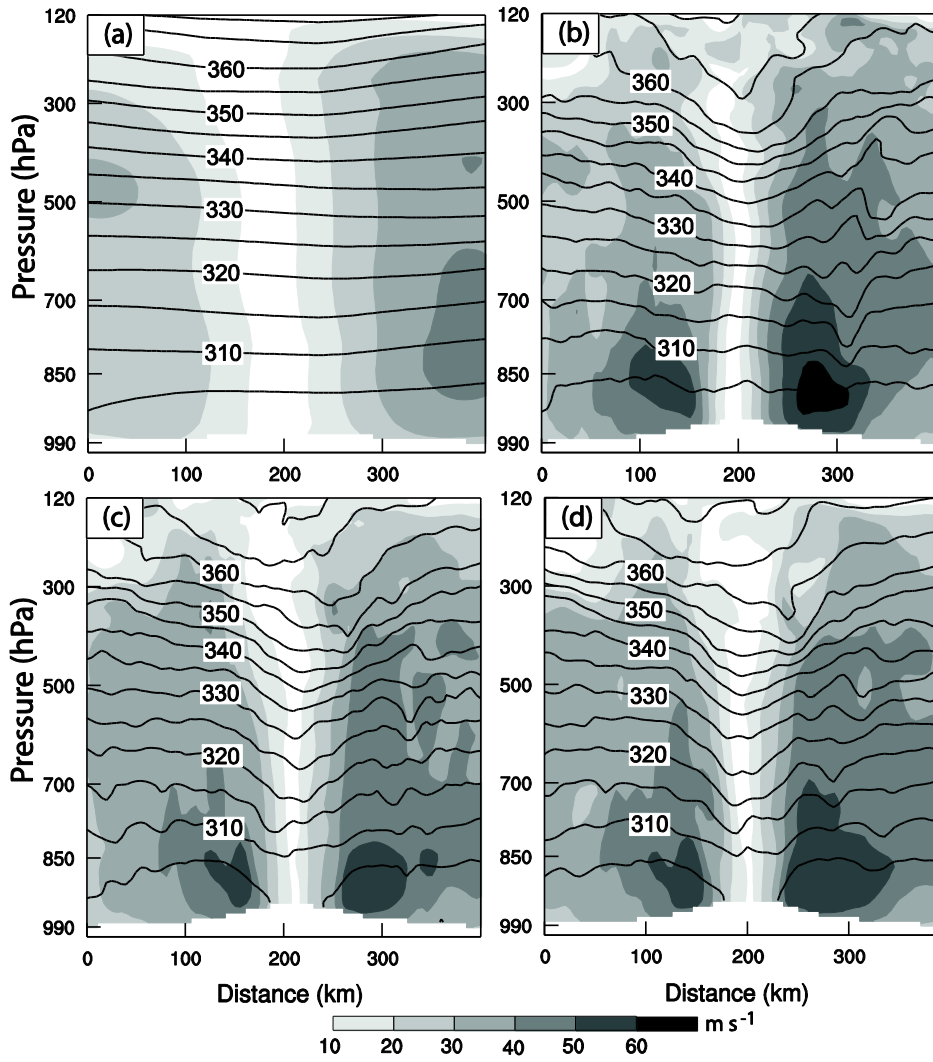
984

985

986

987

988



989

990

991 Fig. 10. Vertical cross sections of analyzed horizontal wind speed (interval of 10 m s^{-1} ,
 992 shaded) and potential temperature (interval of 5 K , solid contours) for (a) NoDA, (b)
 993 3DVARb, (c) HybridF, and (d) HybridH, at 0300 UTC 13 September 2008.

994

995

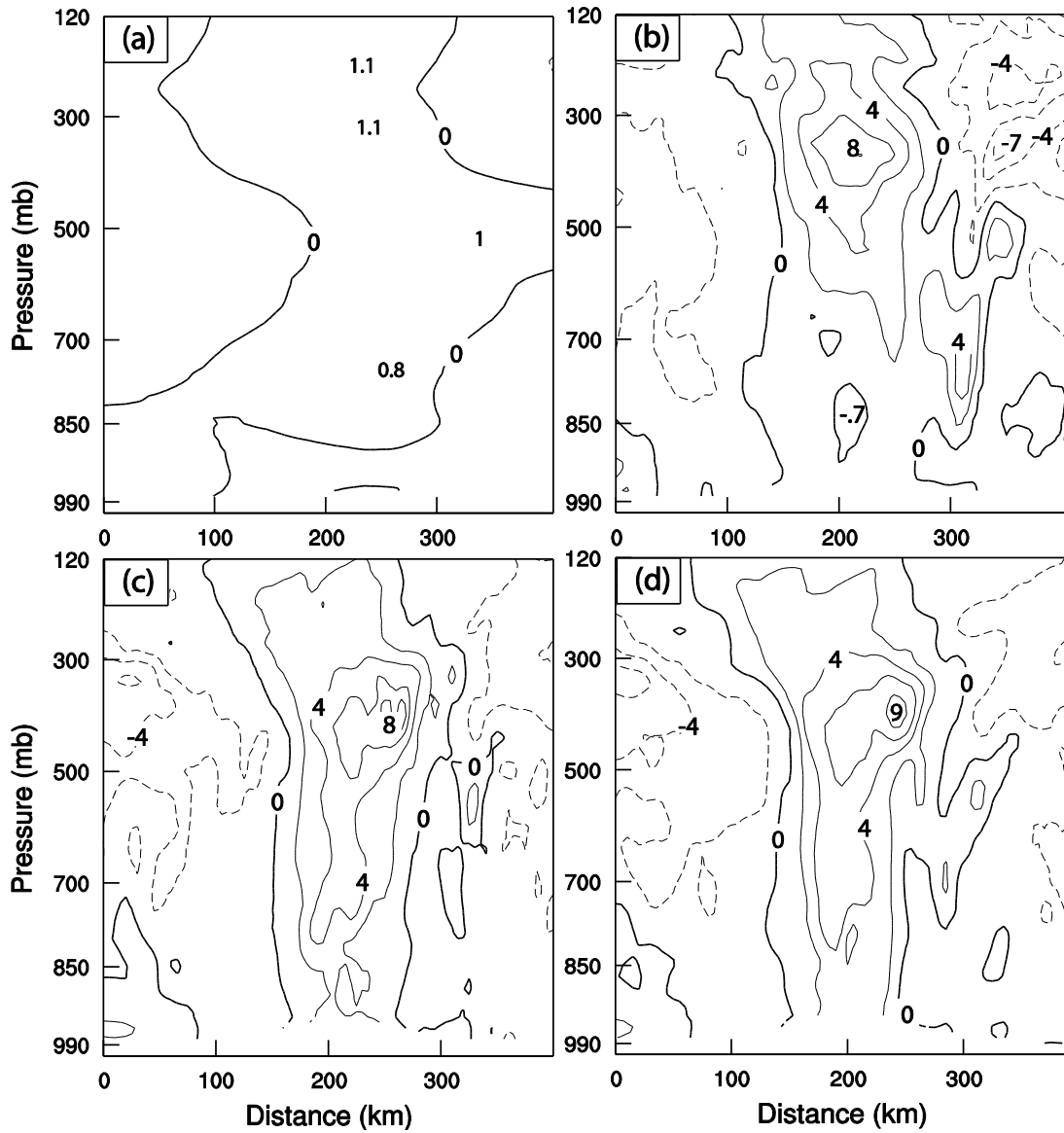
996

997

998

999

1000



1001

1002

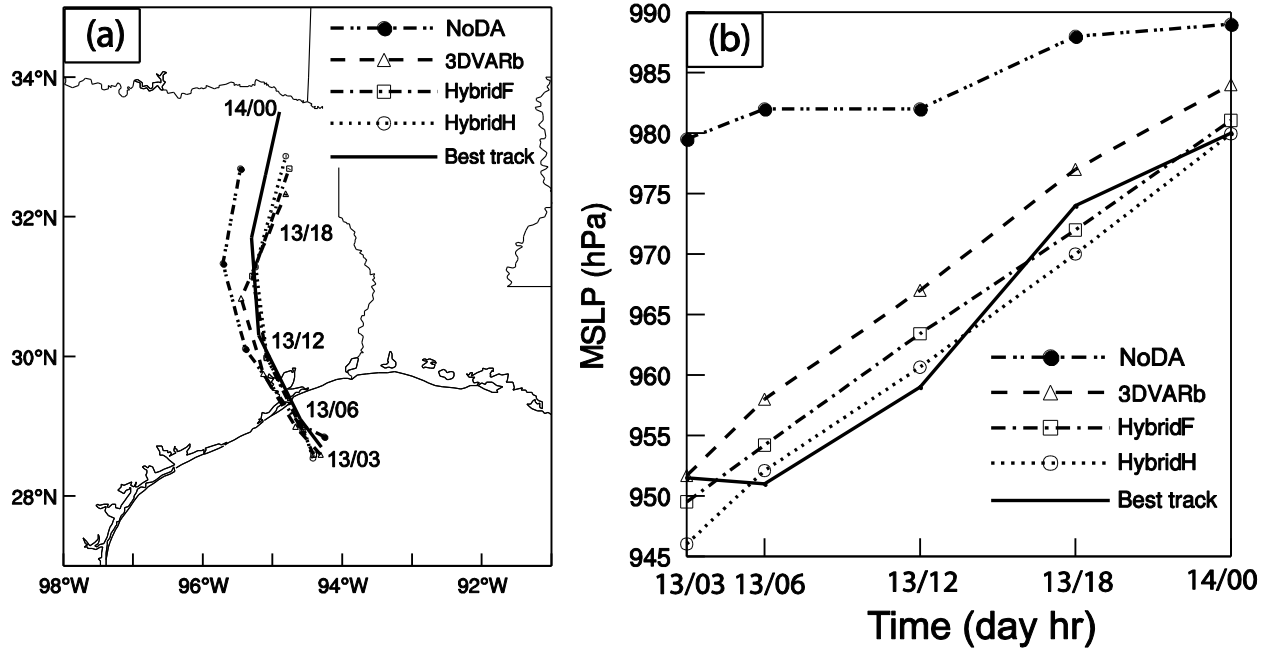
1003 Fig. 11. Vertical cross sections of analyzed temperature anomalies (interval of 2 K)
 1004 for (a) NoDA, (b) 3DVARb, (c) HybridF, and (d) HybridH, at 0300 UTC 13
 1005 September 2008.

1006

1007

1008

1009



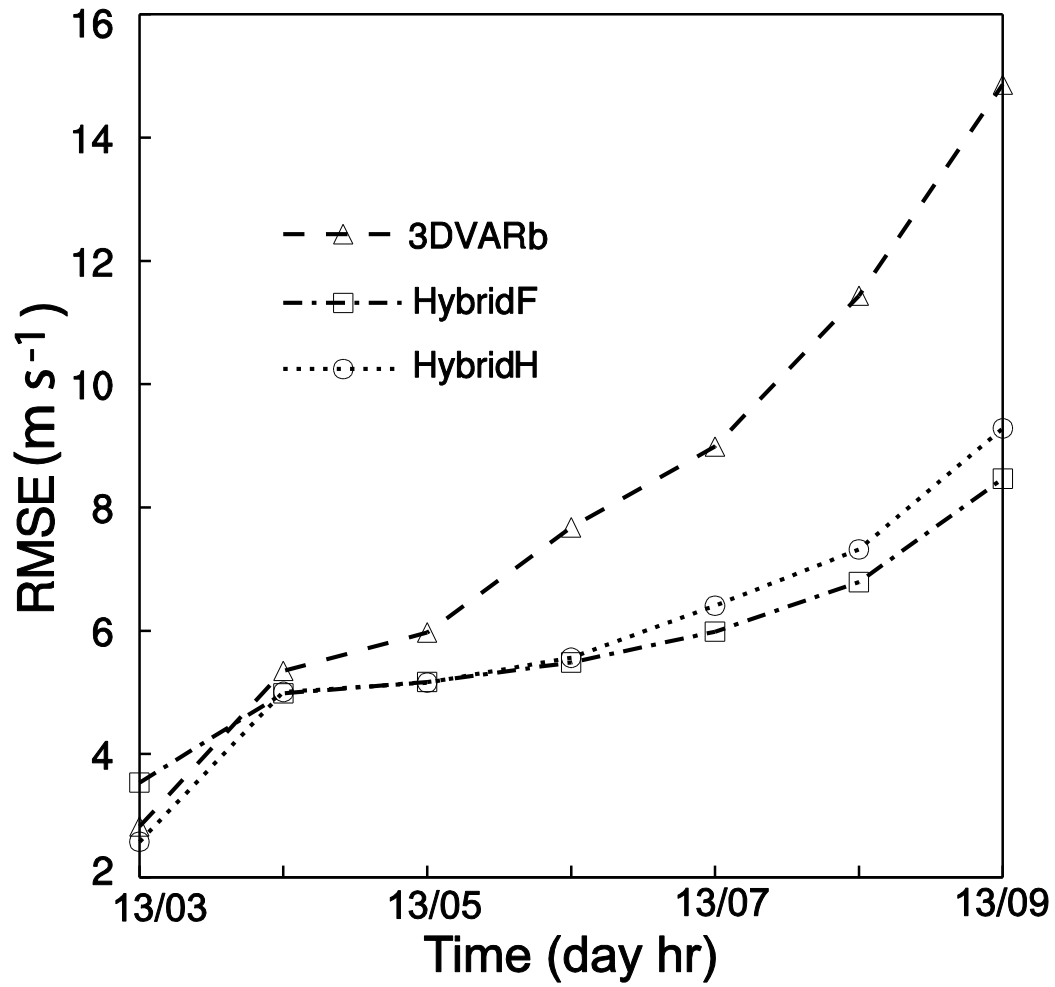
1010

1011

1012 Fig. 12. Deterministic forecast hurricane (a) tracks and (b) minimum sea level
 1013 pressure (hPa) by NoDA, 3DVARb, HybridF, and HybridH as compared to NHC best
 1014 track estimates from 0300 UTC 13 through 0000 UTC 14 September 2008.

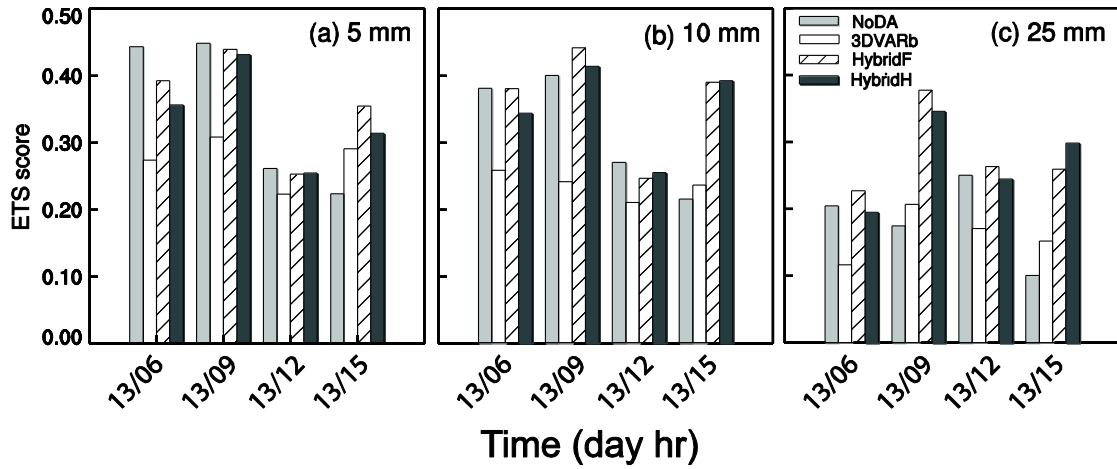
1015

1016



1017
 1018
 1019
 1020
 1021
 1022
 1023
 1024
 1025
 1026
 1027
 1028
 1029
 1030
 1031

Fig. 13. Deterministic forecast RMSEs of V_r (m s^{-1}) by 3DVARb, HybridF, and HybridH from 0300 to 0900 UTC 13 September 2008.



1032

1033

1034 Fig. 14. The equitable threat scores for 3 h accumulated forecast precipitation by
 1035 NoDA, 3DVARb, HybridF, and HybridH at thresholds (a) 5 mm, (b) 10 mm, and (c)
 1036 25 mm, verified against NCEP Stage-IV precipitation analyses valid at 0600, 0900,
 1037 1200, and 1500 UTC 13 September 2008.

1038

1039

1040

1041

1042

1043

1044

1045

1046

1047

1048

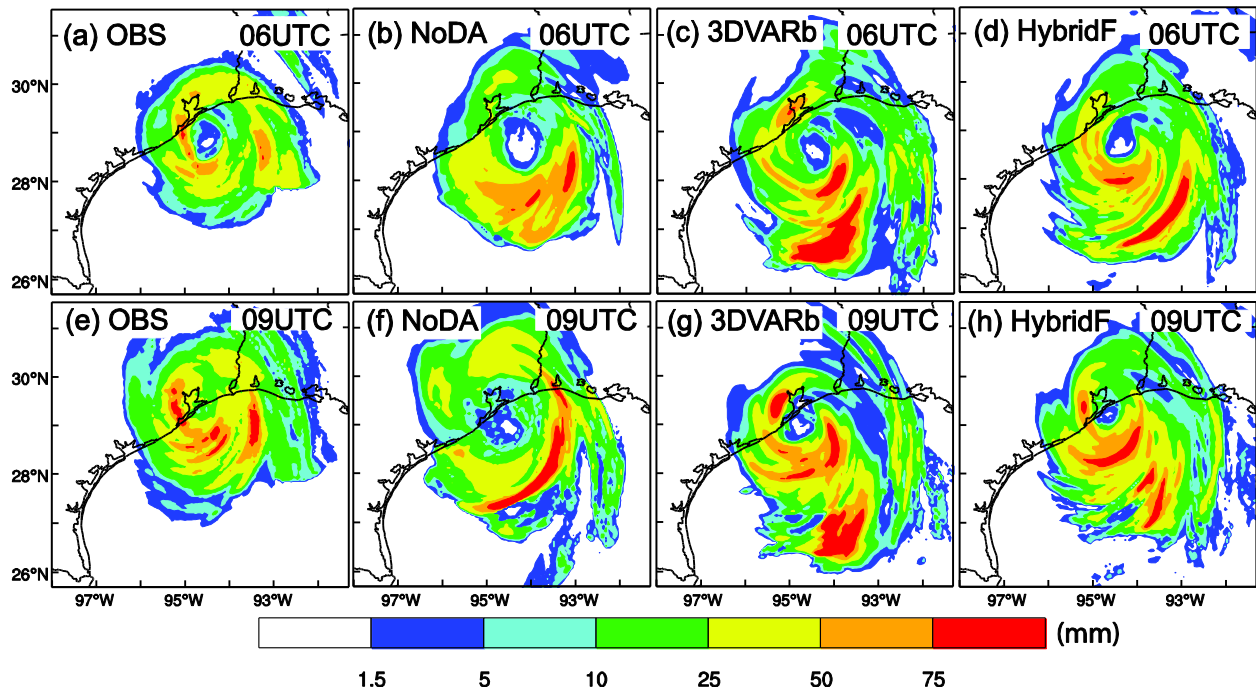
1049

1050

1051

1052

1053



1054

1055

1056

1057

1058

1059

1060

1061

1062

1063

1064

Fig. 15 Three-hour accumulated precipitation (mm) by (1st column) NCEP Stage-IV precipitation analyses, (2nd column) NoDA, (3rd column) 3DVARb, and (4th column) HybridF valid at (top) 0600 and (bottom) 0900 UTC 13 September 2008.